

Living on the edge : ground-state selection in “quantum spin-ice” pyrochlores

Han Yan,^{1,2} Owen Benton,^{1,3} Ludovic Jaubert,^{1,4} and Nic Shannon^{1,2,3}

¹*Okinawa Institute of Science and Technology, Onna-son, Okinawa 904-0412, Japan*

²*Clarendon Laboratory, University of Oxford, Parks Rd., Oxford OX1 3PU, UK*

³*H. H. Wills Physics Laboratory, University of Bristol, Tyndall Av, Bristol BS8-1TL, UK*

⁴*Rudolf Peierls Centre for Theoretical Physics, University of Oxford, 1-6 Keeble Rd, Oxford OX1 3NP, UK*

(Dated: November 6, 2018)

The search for new quantum phases, especially in frustrated magnets, is central to modern condensed matter physics. One of the most promising places to look is in rare-earth pyrochlore magnets with highly-anisotropic exchange interactions, materials closely related to the spin ices $\text{Ho}_2\text{Ti}_2\text{O}_7$ and $\text{Dy}_2\text{Ti}_2\text{O}_7$. Here we establish a general theory of magnetic order in these materials. We find that many of their most interesting properties can be traced back to the “accidental” degeneracies where phases with different symmetry meet. These include the ordered ground state selection by fluctuations in $\text{Er}_2\text{Ti}_2\text{O}_7$, the “dimensional-reduction” observed in $\text{Yb}_2\text{Ti}_2\text{O}_7$, and the absence of magnetic order in $\text{Er}_2\text{Sn}_2\text{O}_7$.

PACS numbers: 74.20.Mn, 11.15.Ha, 75.10.Jm

Like high-energy physics, condensed matter physics is dominated by the idea of symmetry. Any physical property which *cannot* be traced back to a broken symmetry is therefore of enormous fundamental interest. In this context, the spin liquid phases found in frustrated magnets are a rich source of inspiration¹. Perhaps the most widely studied examples are the “spin ice” states in $\text{Ho}_2\text{Ti}_2\text{O}_7$ and $\text{Dy}_2\text{Ti}_2\text{O}_7$, classical spin-liquids famous for their magnetic monopole excitations². And there is now good reason to believe that a *quantum* spin-liquid phase, in which the magnetic monopoles are elevated to the role of “elementary” particles, could exist in spin-ice like materials where quantum effects play a larger role³⁻⁹.

Fortunately there are a wide range of materials in which to look for such a state. The best candidates for a “quantum spin ice” are rare-earth pyrochlore oxides $\text{R}_2\text{A}_2\text{O}_7$ in which the magnetic ions have a doublet ground state, and highly-anisotropic exchange interactions. The physical properties of these materials depend on the choice of rare-earth R^{3+} and transition metal A^{4+} , and are fabulously diverse^{10,11}. In addition to spin ices, this family includes a wide range of systems that order magnetically, spin glasses and systems where local moments couple to itinerant electrons. And significantly, a number of materials, including $\text{Tb}_2\text{Ti}_2\text{O}_7$ [12,13] and $\text{Er}_2\text{Sn}_2\text{O}_7$ [14–18] have never been seen to order at *any* temperature.

In this article we single out two of the best-characterised examples of rare-earth pyrochlore magnets, $\text{Er}_2\text{Ti}_2\text{O}_7$ and $\text{Yb}_2\text{Ti}_2\text{O}_7$, and explore how their properties fit into the “bigger picture” of magnetism on the pyrochlore lattice. We find that both the “order by disorder” ground-state selection in $\text{Er}_2\text{Ti}_2\text{O}_7$ ¹⁹, and the “dimensional reduction” observed in $\text{Yb}_2\text{Ti}_2\text{O}_7$ ²⁰, can be understood in terms of proximity to nearby zero-temperature phase transitions. In the process, we establish a general phase diagram for magnetic order in pyrochlore magnets with anisotropic exchange interactions,

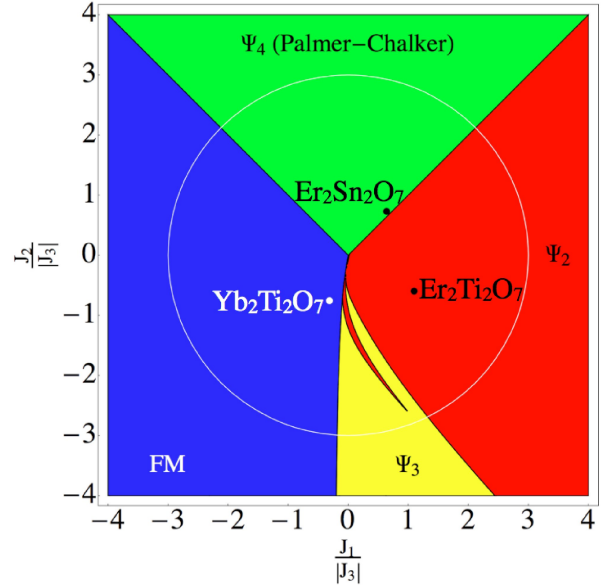


FIG. 1: Classical ground state phase diagram for a pyrochlore magnet with anisotropic exchange interactions. The model considered is the most general nearest-neighbour exchange Hamiltonian on the pyrochlore lattice \mathcal{H}_{ex} [Eq. (1)], with ferromagnetic “pseudo-dipolar” interaction ($J_3 < 0$), and vanishing Dzyaloshinskii-Moriya interactions ($J_4 = 0$). There are four distinct ordered phases, illustrated in the insets to Fig. 2. Points correspond to known parameters for $\text{Yb}_2\text{Ti}_2\text{O}_7$ [26], $\text{Er}_2\text{Ti}_2\text{O}_7$ [28], and $\text{Er}_2\text{Sn}_2\text{O}_7$ [18], setting $J_4 = 0$.

and identify where these ordered states might give way to unconventionally ordered or spin liquid phases. These results place a third material, $\text{Er}_2\text{Sn}_2\text{O}_7$ [18], tantalizingly close to a region of quantum disorder.

The physics driving the spin-ice state in $\text{Ho}_2\text{Ti}_2\text{O}_7$ and $\text{Dy}_2\text{Ti}_2\text{O}_7$ is predominantly classical. In these materials,

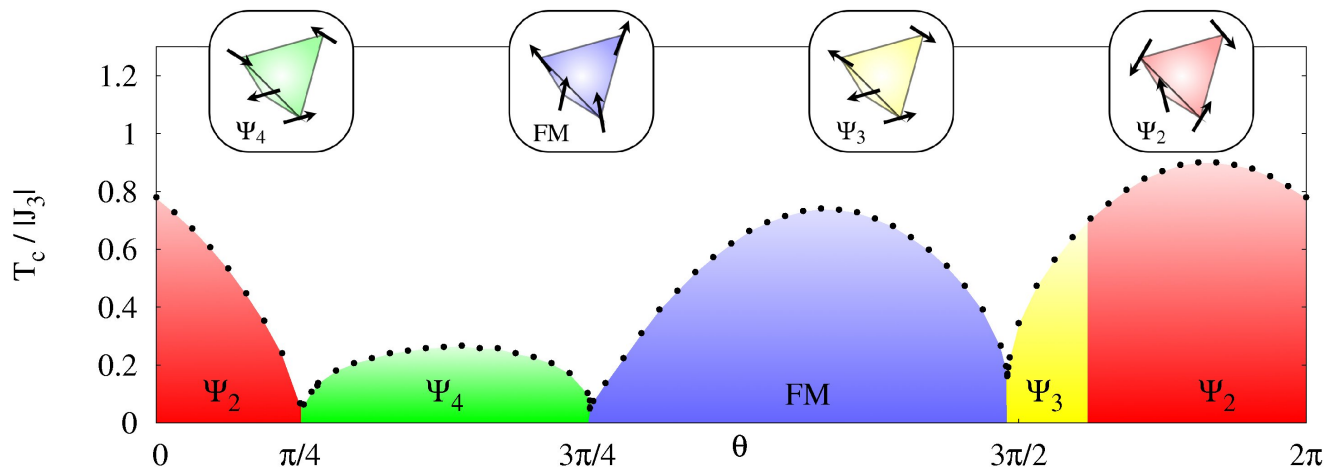


FIG. 2: Finite-temperature phase diagram for pyrochlore magnet with anisotropic exchange interactions. The model considered is \mathcal{H}_{ex} [Eq. (1)], with $J_1 = 3|J_3|\cos\theta$, $J_2 = 3|J_3|\sin\theta$, $J_3 < 0$, and $J_4 \equiv 0$, corresponding to the white circle in Fig. 1. Points show finite temperature phase transitions found from classical Monte Carlo simulation, as described in the supplementary information. The four ordered phases, Palmer-Chalker (Ψ_4), non-collinear ferromagnetic (FM), coplanar antiferromagnetic (Ψ_3) and non-coplanar antiferromagnetic (Ψ_2), are illustrated at the top of the figure. Each of these phases is six-fold degenerate, with zero crystal momentum, and is completely specified by the spin configuration in a single tetrahedron.

the magnetic ions have Ising moments of $\sim 10\mu_b$, which couple through dipolar interactions^{21,22}. In contrast, the magnetic ions in $\text{Yb}_2\text{Ti}_2\text{O}_7$ and $\text{Er}_2\text{Ti}_2\text{O}_7$ have a doublet ground state with XY character, and relatively small effective moment^{10,23}. In this case, quantum effects play a much larger role, and interactions between spins can be described by an anisotropic nearest-neighbour exchange Hamiltonian^{24–30}

$$\mathcal{H}_{\text{ex}} = \sum_{\langle ij \rangle} J_{ij}^{\mu\nu} S_i^\mu S_j^\nu \quad (1)$$

where the sum on $\langle ij \rangle$ runs over the bonds of the pyrochlore lattice. The cubic symmetry of the pyrochlore lattice permits only four independent parameters to enter the matrix $J_{ij}^{\mu\nu}$ ²⁴, and for a bond directed along $(0, -1, -1)$ this is given by

$$\mathbf{J}_{01} = \begin{pmatrix} J_2 & J_4 & J_4 \\ -J_4 & J_1 & J_3 \\ -J_4 & J_3 & J_1 \end{pmatrix} \quad (2)$$

with the corresponding matrix for all other bonds found by applying lattice symmetry operations.

This model supports an extremely rich variety of different ground states. For $J_1 = -J_2 = J_3 = J_4 = -1/3$, \mathcal{H}_{ex} [Eq. (1)] favours the “ice rules” states found in $\text{Ho}_2\text{Ti}_2\text{O}_7$ and $\text{Dy}_2\text{Ti}_2\text{O}_7$ [31–33]. Quantum tunnelling between these states gives rise to a “U(1)” quantum spin liquid with photon-like excitations^{3,4,6,7}, and at a mean-field level, this is the ground state of \mathcal{H}_{ex} for a moderately wide range of (J_1, J_2, J_3, J_4) [5,8,9]. Meanwhile, for $J_1 = J_2 = J$, and $J_3 = J_4 = 0$, \mathcal{H}_{ex} reduces to the Heisenberg model on a pyrochlore lattice, also studied as a quantum spin-liquid^{34,35}. Nonetheless, materials such as $\text{Er}_2\text{Ti}_2\text{O}_7$

— which is extremely well-described by \mathcal{H}_{ex} ^{28–30} — do order magnetically¹⁹.

Since \mathcal{H}_{ex} [Eq. (1)] does not, in general, possess *any* continuous spin-rotation symmetry, different ordered phases can be characterised by the lattice symmetries which they break. Moreover, the model \mathcal{H}_{ex} [Eq. (1)] has the remarkable property that it is *always* possible to find a classical ground state with $\mathbf{q} = 0$, i.e. one in which the spin-configuration in a single four-site unit cell is repeated across the entire lattice (a proof of this statement is given in the supplementary information). The great richness of the problem stems from the fact that this does *not* preclude the existence of other, degenerate, ground states at finite \mathbf{q} , or of a continuous ground-state manifold at $\mathbf{q} = 0$.

In fact, where the different ground states of a single tetrahedron are linked by a symmetry which leaves at least one spin unchanged, we find that it is *always* possible to construct alternative ground states with finite \mathbf{q} . Such “accidental” degeneracies are common, and we will argue below that they drive not only the spin-liquid phases of \mathcal{H}_{ex} [Eq. (1)], but also many of the interesting phenomena associated with ordered phases.

Considering first what happens for $\mathbf{q} = 0$, we find that \mathcal{H}_{ex} [Eq. (1)] supports four distinct classes of magnetically ordered ground state, transforming like the A_2 , E , T_2 , and T_1 irreducible representations of the point group of a tetrahedron, T_d . The Hamiltonian \mathcal{H}_{ex} [Eq. (1)] can be expressed in terms of the associated order parameters \mathbf{m}_λ

$$\mathcal{H}_{\text{ex}}^{[T_d]} = \frac{1}{2} \left[a_{A_2} m_{A_2}^2 + a_E \mathbf{m}_E^2 + a_{T_2} \mathbf{m}_{T_2}^2 + a_{T_{1,A}} \mathbf{m}_{T_{1,A}}^2 + a_{T_{1,B}} \mathbf{m}_{T_{1,B}}^2 + a_{T_{1,AB}} \mathbf{m}_{T_{1,A}} \cdot \mathbf{m}_{T_{1,B}} \right]. \quad (3)$$

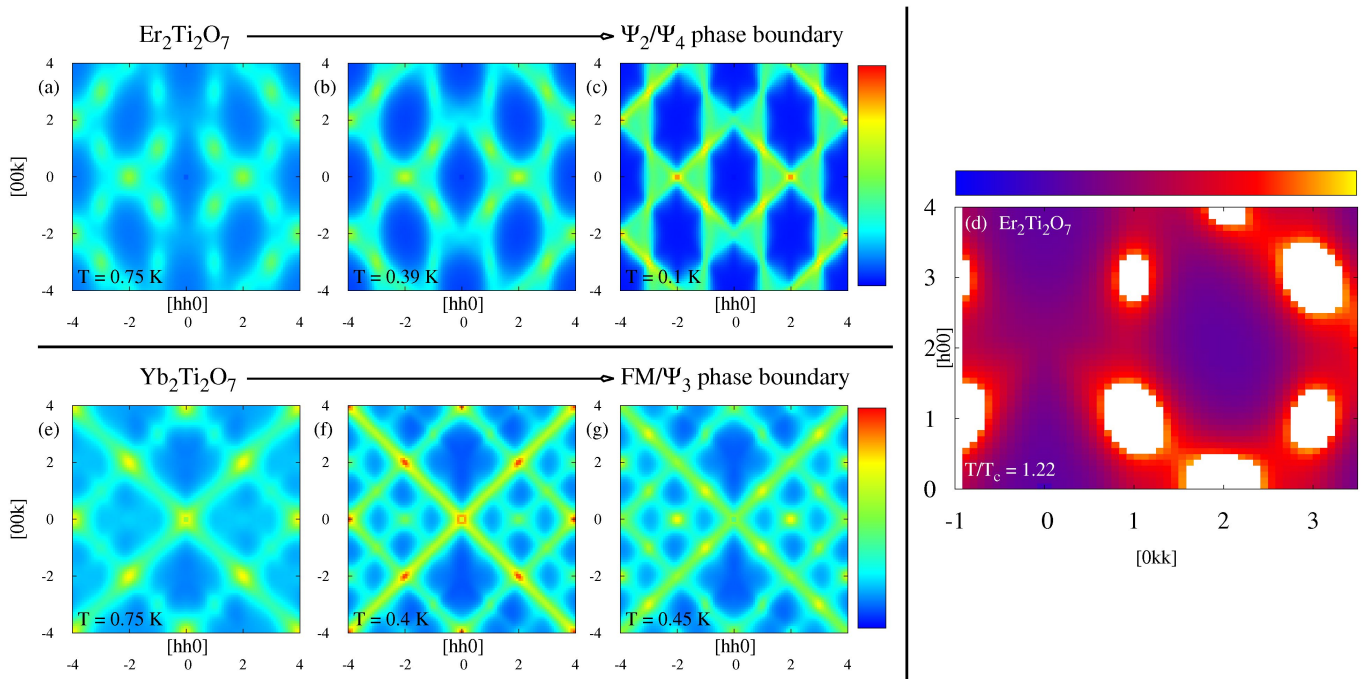


FIG. 3: Correlations in the high-temperature paramagnetic phase, as revealed by the quasi-elastic structure factor $S(\mathbf{q})$. (a-c) results for parameters interpolating from (a) $\text{Er}_2\text{Ti}_2\text{O}_7$ [28] to (c) the boundary of the Palmer-Chalker phase (Ψ_4). The diffuse scattering characteristic of the Ψ_2 phase evolve into sharp features reminiscent of pinch points when bordering the Ψ_4 phase. (d) detail of $S(\mathbf{q})$ for parameters appropriate to $\text{Er}_2\text{Ti}_2\text{O}_7$, plotted with a colour scale chosen to match Fig. 14 of [42]. Results are taken from classical Monte Carlo simulations carried out for (a) $J_2 = -0.06$ mK, $T = 750$ mK; (b) $J_2 = 0.06$ mK, $T = 390$ mK; (c) $J_2 = 0.11$ mK, $T = 100$ mK. (d) $J_2 = -0.06$ mK, $T = 616$ mK. In all cases, $J_1 = -0.11$ mK, $J_3 = -0.1$ mK, $J_4 \equiv 0$, and $S(\mathbf{q})$ has been calculated using g-tensor appropriate to $\text{Er}_2\text{Ti}_2\text{O}_7$ [28]. (e-g) results for parameters interpolating from $\text{Yb}_2\text{Ti}_2\text{O}_7$ [cf. Ref. (26)], to the border of the Ψ_3 phase. The rods of scattering along $[111]$ directions, interpreted as evidence of dimensional reduction in $\text{Yb}_2\text{Ti}_2\text{O}_7$ [44], evolve into weakly-dispersing, low-energy excitations in the neighbouring Ψ_3 phase. Results are taken from classical Monte Carlo simulations of \mathcal{H}_{ex} [Eq. (1)] for (e) $J_1 = -0.09$ meV, $T = 750$ mK; (f) $J_1 = -0.04$ meV, $T = 400$ mK; (g) $J_1 = -0.0288$ meV, $T = 450$ mK. In all cases, $J_2 = -0.22$ meV, $J_3 = -0.29$ meV, $J_4 \equiv 0$, and $S(\mathbf{q})$ has been calculated using g-tensor appropriate to $\text{Yb}_2\text{Ti}_2\text{O}_7$ [47].

where the order parameters \mathbf{m}_λ and coefficients $a_\lambda = a_{\lambda,1}J_1 + a_{\lambda,2}J_2 + a_{\lambda,3}J_3 + a_{\lambda,4}J_4$ are defined in the supplementary information. For classical spins this model must be solved subject to the constraints that each spin is separately normalised to $\mathbf{S}^2 = S^2$. We note that it is also possible to derive $\mathcal{H}_{\text{ex}}^{[\text{T}_d]}$ as the $\mathbf{q} = 0$ limit of a classical field theory reminiscent of electromagnetism. This approach will be developed further elsewhere.

Starting from $\mathcal{H}_{\text{ex}}^{[\text{T}_d]}$ [Eq. (3)], it is possible to find which form of 4-sublattice order has the lowest energy for *any* given set of parameters (J_1, J_2, J_3, J_4). However $\text{Yb}_2\text{Ti}_2\text{O}_7$ [26], $\text{Er}_2\text{Ti}_2\text{O}_7$ [28] and $\text{Er}_2\text{Sn}_2\text{O}_7$ [18] all have ferromagnetic pseudodipolar interaction $J_3 < 0$, and small Dzyaloshinskii-Moriya interaction $J_4 \ll |J_1|, |J_2|, |J_3|$. In what follows, we therefore concentrate on the most general form of ground state possible for $J_3 < 0$ and $J_4 \equiv 0$. Our results are summarised in Fig. 1.

We find four distinct ordered phases, which we label following the conventions of [37,51]: i) Ψ_4 — a coplanar antiferromagnetic “Palmer-Chalker” [38] phase,

transforming with T_2 ; ii) FM — a non-collinear phase with finite magnetisation, transforming with T_1 . This is the ground state for parameters appropriate to $\text{Yb}_2\text{Ti}_2\text{O}_7$ [26] or $\text{Yb}_2\text{Sn}_2\text{O}_7$ [39]; iii) Ψ_3 — a coplanar antiferromagnetic phase, selected by fluctuations from a one-dimensional manifold of states transforming with E . This state was among those enumerated by Bramwell, Gingras and Reimers⁴⁰; iv) Ψ_2 — a non-coplanar antiferromagnetic phase, selected by fluctuations from the same one-dimensional manifold of states as Ψ_3 . This phase is the known ground state in $\text{Er}_2\text{Ti}_2\text{O}_7$ [19], originally studied by Champion and Holdsworth in the context of a Heisenberg model with single-ion anisotropy⁴¹. Each of these phases singles out a unique $[100]$ axis, and is six-fold degenerate. The $T \rightarrow 0$ phase boundary between the Ψ_2 and Ψ_3 phases in Fig. 1 was determined using classical spin-wave theory; analytic expressions for all the other phase boundaries are given in the supplementary information. Ground state spin configurations for each of these phases are shown in Fig. 2.

We have also explored the finite-temperature evolution of these phases using classical Monte Carlo simula-

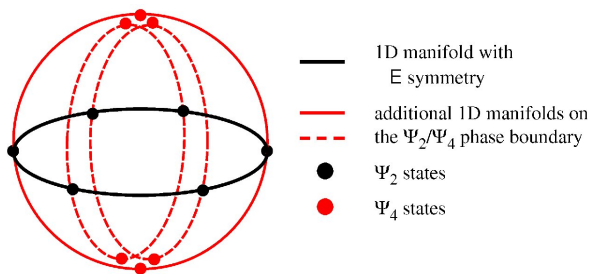


FIG. 4: Structure of the $\mathbf{q} = 0$ classical ground-state manifold at the boundary between the Palmer-Chalker phase (Ψ_4), and the one-dimensional manifold of states with \mathbf{E} symmetry. The black circle denotes the manifold of \mathbf{E} -symmetry ground states, including the six Ψ_2 ground states (black dots). These are connected to the six Ψ_4 ground states with T_2 symmetry (red dots), by three, additional, one-dimensional manifolds (solid and dashed red lines).

tion. These results are summarised in Fig. 2. The most striking feature of simulations is the complex evolution of correlations in the paramagnetic phase, highlighted in Fig. 3.

While these results provide an important context for experiment, they leave unanswered the important question of *why* fluctuations favour Ψ_2 for parameters appropriate to $\text{Er}_2\text{Ti}_2\text{O}_7$ ^{28,29}, and Ψ_3 elsewhere. Similarly, knowing that $\text{Yb}_2\text{Ti}_2\text{O}_7$ might be expected to order ferromagnetically does little to explain the apparent dimensional-reduction seen in its paramagnetic phase^{20,44}. And the absence of magnetic order in $\text{Er}_2\text{Sn}_2\text{O}_7$ remains mysterious. The key to understanding all of these problems lies in the structure of the ground state manifold where phases with different symmetry meet.

Let us first consider $\text{Er}_2\text{Ti}_2\text{O}_7$. Early heat capacity measurement of $\text{Er}_2\text{Ti}_2\text{O}_7$ revealed a transition at $T_c = 1.25$ K, releasing an entropy $\Delta s \approx 0.97k_B \ln 2$ per spin, consistent with the ordering of the ground state doublet of Er^{10} . Later work identified this transition as a textbook example of “order by disorder”, with fluctuations selecting a Ψ_2 ground state from a continuous manifold of states with local easy-plane character^{19,25,28,29}. Using parameters taken from [28], we have confirmed that $\text{Er}_2\text{Ti}_2\text{O}_7$ lies within a Ψ_2 phase. Estimates from our classical Monte Carlo simulations give $T_c \approx 500\text{mK}$, somewhat lower than in experiment, but with excellent agreement with experimental measurements⁴² of $S(\mathbf{q})$ within the paramagnetic state [Fig. 3(d)]. However these parameters also place $\text{Er}_2\text{Ti}_2\text{O}_7$ relatively close to the boundary with the neighbouring Palmer-Chalker phase [cf. Fig. 1]

On this boundary, we find that it is possible to deform the ground state continuously from Ψ_2 to a corresponding Palmer-Chalker state. In more formal terms, the ground state of $\mathcal{H}_{\text{ex}}^{[\text{T}d]}$ [Eq. (3)] is enlarged from a single one-dimensional manifold connecting the Ψ_2 and Ψ_3 states, to a set of connected one-dimensional mani-

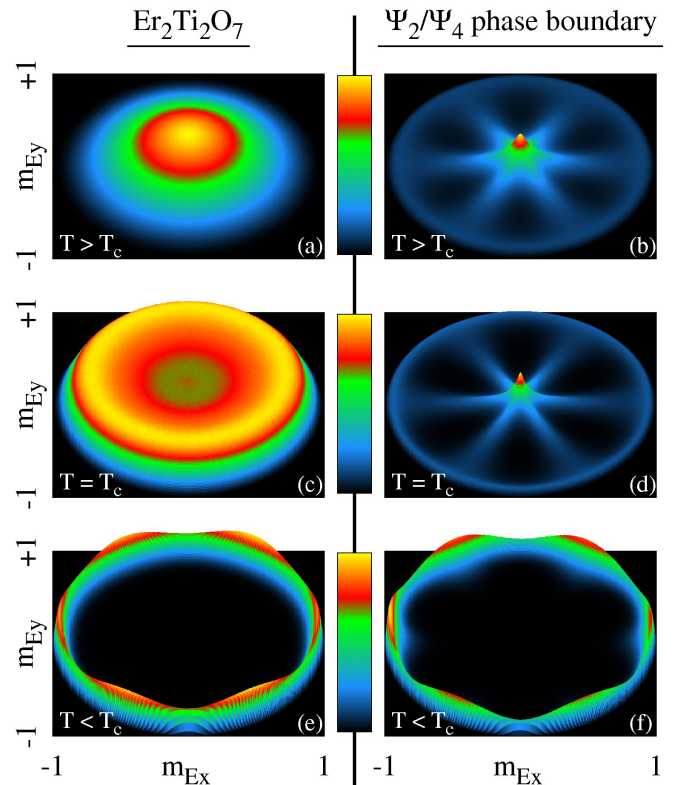


FIG. 5: Selection of the Ψ_2 ground state by thermal fluctuations, as revealed by the probability density $P(\mathbf{m}_{\mathbf{E}})$. (a, c, e) results for parameters appropriate to $\text{Er}_2\text{Ti}_2\text{O}_7$ [28], setting $J_4 = 0$. (b, d, f) results for parameters bordering the Palmer-Chalker (Ψ_4) ground state. (a) broad distribution of fluctuations for $T > T_c$. (b) “spoked wheel” pattern, characteristic of the enlarged ground-state manifold [Fig. 4], visible even for $T > T_c$. (c) emergence of a one-dimensional manifold of states at $T = T_c$. (d) emergence of a one-dimensional manifold of states at $T = T_c$, showing branching at the six Ψ_2 states. (e) selection of six Ψ_2 ground states within the manifold for $T < T_c$. (f) selection of six Ψ_2 ground states within the manifold for $T < T_c$. Results are taken from classical Monte Carlo simulations of \mathcal{H}_{ex} [Eq. (1)], with parameters described in the supplementary information.

folds, which also interpolate to the Palmer-Chalker states [Fig. 4]. Since these manifolds branch at Ψ_2 , Ψ_2 gains an additional soft set of excitations, and therefore has a lower free energy than Ψ_3 . These arguments remain valid at finite temperature [Fig. 5], and in the presence of quantum fluctuations, which are already known to favour Ψ_2 order [25,28,29]. We can therefore understand the “order by disorder” selection Ψ_2 in $\text{Er}_2\text{Ti}_2\text{O}_7$ from its proximity to the Palmer-Chalker phase.

We note that an exactly parallel argument predicts that Ψ_3 should be favoured approaching the boundary with the ferromagnet [cf. Fig. 1]. Where these two phase boundaries approach one another, the soft modes associated with the two different sets of manifolds compete. This leads to the complicated, re-entrant behaviour seen

in Fig. 1, and studied for quantum spins in [43].

We now turn to $\text{Yb}_2\text{Ti}_2\text{O}_7$. Quasi-elastic neutron scattering from the paramagnetic phase of $\text{Yb}_2\text{Ti}_2\text{O}_7$ is dominated by dramatic “rod”-like features in the [111] directions of reciprocal space. First observed almost ten years ago⁴⁵, these rods of scattering have since been interpreted as evidence of dimensional reduction^{20,44} and, in the context of \mathcal{H}_{ex} [Eq. (1)], as evidence of significant anisotropic exchange interactions^{26,46}. They are a robust feature of $S(\mathbf{q})$, as calculated from \mathcal{H}_{ex} [Eq. (1)] within both the (semi-classical) random phase approximation^{46,48}, and classical Monte Carlo simulation [Fig. 3]. However, despite their ubiquity, the origin of these rods of scattering remains mysterious.

Dimensional reduction is a well-defined feature of \mathcal{H}_{ex} [Eq. (1)]. The classical ground states of \mathcal{H}_{ex} reduce to a set of independent kagome planes on the boundary between FM and Palmer-Chalker phases, and to a set of independent chains on the boundary between the Ψ_2 and Palmer-Chalker phases. However the rods of scattering seen in $\text{Yb}_2\text{Ti}_2\text{O}_7$ occur for parameters where the ground state of \mathcal{H}_{ex} is expected to be ordered and fully three-dimensional. They can instead be traced back to dimensionally-reduced excitations — quasi-degenerate lines of low-lying spin wave excitations, which evolve into low-lying excitations of Ψ_3 on the boundary between the FM and the Ψ_3 phases. This progression is clear in the evolution of $S(\mathbf{q})$ from parameters appropriate to $\text{Yb}_2\text{Ti}_2\text{O}_7$ [Fig. 3(e)] to the border of the Ψ_3 phase [Fig. 3(g)].

Our classical Monte Carlo simulations predict that $\text{Yb}_2\text{Ti}_2\text{O}_7$ orders at 450 mK, a little higher than the $T_c \approx 250$ mK found in those samples which show a phase transition^{10,44,48}. We note that the detailed form of $S(\mathbf{q})$ observed in those samples of $\text{Yb}_2\text{Ti}_2\text{O}_7$ which do *not* exhibit a phase transition^{20,44,49} is closer to predictions bordering on the Ψ_3 phase [Fig. 3(f)–(g)], than to those for the parameters given in²⁶ [Fig. 3(e)]. In particular, the noticeable enhancement of scattering at [220] offers strong evidence for the proximity of a Ψ_3 phase. It is therefore interesting to ask what effect disorder^{49,50}, and quantum fluctuations, have on the ground state of \mathcal{H}_{ex} [Eq. (1)]?

We have explored the effect of quantum fluctuations on each of the four ground states of \mathcal{H}_{ex} [Eq. (1)], within linear spin wave theory. These results are summarised in Fig. 6. As expected, the enlargement of the ground state manifold at phase boundaries has a profound influence on fluctuations, eliminating order entirely for a wide range of parameters. This tendency is most pronounced where the symmetry of the model is highest, e.g. near the high symmetry point $|(J_1, J_2)|/|J_3| \rightarrow 0$, and approaching the Heisenberg line $J_1 = J_2, J_3 = J_4 = 0$. However, deep within the ordered phases, all excitations are gapped, and the ordered moment approaches its full, classical, value.

The implications of these results for $\text{Er}_2\text{Sn}_2\text{O}_7$ are striking. Like $\text{Er}_2\text{Ti}_2\text{O}_7$ and $\text{Yb}_2\text{Ti}_2\text{O}_7$, the magnetic ions in $\text{Er}_2\text{Sn}_2\text{O}_7$ have a Kramers doublet ground state¹⁴,

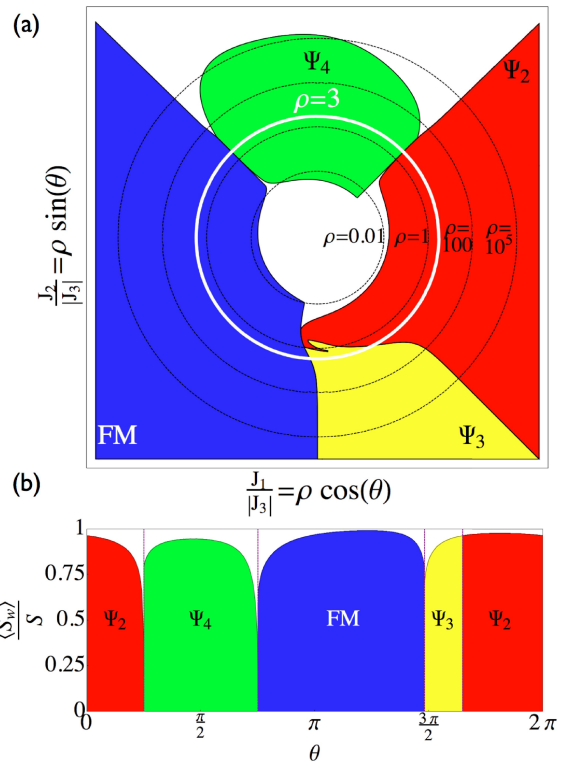


FIG. 6: Effect of quantum fluctuations on magnetic order. (a) Ground-state phase diagram for a pyrochlore magnet with anisotropic exchange interactions, plotted in log-polar coordinates. Blank regions indicate where magnetic order is entirely eliminated by quantum fluctuations. (b) Fraction of full classical moment achieved in ordered phases, for $J_1 = 3|J_3|\cos\theta$, $J_2 = 3|J_3|\sin\theta$. Away from phase boundaries, the ordered moment is close to its full classical value. All results are obtained within linear spin-wave theory for \mathcal{H}_{ex} [Eq. (1)], setting $J_3 < 0$ and $J_4 \equiv 0$.

and are believed to be well-described by \mathcal{H}_{ex} [Eq. (1)] [18]. Correlations reminiscent of the Palmer-Chalker phase have been observed in neutron scattering¹⁸, and magnetization measurements show some evidence of spin-freezing at low temperatures¹⁸. Nonetheless, $\text{Er}_2\text{Sn}_2\text{O}_7$ shows *no* evidence of magnetic order, in thermodynamic measurements^{17,18}, μSR ¹⁵, or neutron scattering^{17,18}, down to a temperature of 20 mK¹⁵.

Our ground state analysis places $\text{Er}_2\text{Sn}_2\text{O}_7$ extremely close to the boundary between Ψ_4 and Ψ_2 [Fig. 1]. Classical Monte Carlo simulations, using parameters taken from¹⁸, predict a transition into Palmer-Chalker (Ψ_4) state at $T_c = 204 \pm 5$ mK. However linear spin-wave theory — which typically *underestimates* quantum effects — predicts that there is a narrow region of disorder between the Ψ_4 and Ψ_2 phases. $\text{Er}_2\text{Sn}_2\text{O}_7$ lies on the edge of this disordered region, and is therefore a strong candidate for a quantum spin liquid.

In conclusion, rare-earth pyrochlore oxides offer a treasure-trove of different magnetic phases, including both classical and quantum spin liquids. In this article

we have established a general theory of magnetic order in materials where exchange interactions are limited to nearest-neighbour bonds. We find that ordered phases of different symmetry are connected by enlarged ground-state manifolds. These “accidental” degeneracies have a profound effect, driving both ground state selection in $\text{Er}_2\text{Ti}_2\text{O}_7$, and the “dimensional-reduction” seen in $\text{Yb}_2\text{Ti}_2\text{O}_7$. They also open the door to quantum spin liquids — a situation which may be realised in $\text{Er}_2\text{Sn}_2\text{O}_7$. In this context, it could be extremely interesting to explore the effect of pressure and chemical substitution on systems like $\text{Yb}_2\text{Ti}_2\text{O}_7$ and $\text{Er}_2\text{Sn}_2\text{O}_7$, living on the edge of conventional magnetic order.

Acknowledgments: The authors are pleased to acknowledge helpful conversations with Bruce Gaulin, Michel Gingras, Edwin Kermarrec, Isabelle Mirebeau, Sylvain Petit, Karlo Penc, and Kate Ross, and a critical reading of the manuscript by Mathieu Taillefumier. This work was supported by OIST.

Appendix A: Definition of model

The pyrochlore lattice is a corner-sharing network of tetrahedra. The lattice has overall cubic symmetry $Fd\bar{3}m$, and is bipartite in tetrahedra, with the centres of the tetrahedra forming a diamond lattice. In what follows, we adopt the convention of numbering the spins in a tetrahedron 0, 1, 2, and 3, as shown in Fig. 7, with sites at positions

$$\begin{aligned} \mathbf{r}_0 &= \left(\frac{1}{2}, \frac{1}{2}, \frac{1}{2} \right), \\ \mathbf{r}_1 &= \left(\frac{1}{2}, -\frac{1}{2}, -\frac{1}{2} \right), \\ \mathbf{r}_2 &= \left(-\frac{1}{2}, \frac{1}{2}, -\frac{1}{2} \right), \\ \mathbf{r}_3 &= \left(-\frac{1}{2}, -\frac{1}{2}, \frac{1}{2} \right). \end{aligned} \quad (\text{A1})$$

relative to the centre of the tetrahedron. The spins at the four sites are denoted as $\mathbf{S}_{i=0,1,2,3}$.

The most general nearest-neighbour exchange Hamiltonian, respecting the symmetry of the pyrochlore lattice, for pseudospin-1/2 variables \mathbf{S}_i representing a Kramers doublet on each site, can be written as²⁴

$$\mathcal{H}_{\text{ex}} = \sum_{\langle ij \rangle} J_{ij}^{\mu\nu} S_i^\mu S_j^\nu \quad (\text{A2})$$

where the sum on $\langle ij \rangle$ runs over the bonds of the pyrochlore lattice and

$$\begin{aligned} \mathbf{J}_{01} &= \begin{pmatrix} J_2 & J_4 & J_4 \\ -J_4 & J_1 & J_3 \\ -J_4 & J_3 & J_1 \end{pmatrix} & \mathbf{J}_{02} &= \begin{pmatrix} J_1 & -J_4 & J_3 \\ J_4 & J_2 & J_4 \\ J_3 & -J_4 & J_1 \end{pmatrix} \\ \mathbf{J}_{03} &= \begin{pmatrix} J_1 & J_3 & -J_4 \\ J_3 & J_1 & -J_4 \\ J_4 & J_4 & J_2 \end{pmatrix} & \mathbf{J}_{12} &= \begin{pmatrix} J_1 & -J_3 & J_4 \\ -J_3 & J_1 & -J_4 \\ -J_4 & J_4 & J_2 \end{pmatrix} \\ \mathbf{J}_{13} &= \begin{pmatrix} J_1 & J_4 & -J_3 \\ -J_4 & J_2 & J_4 \\ -J_3 & J_4 & J_1 \end{pmatrix} & \mathbf{J}_{23} &= \begin{pmatrix} J_2 & -J_4 & J_4 \\ J_4 & J_1 & -J_3 \\ -J_4 & -J_3 & J_1 \end{pmatrix} \end{aligned} \quad (\text{A3})$$

We can characterize the four different exchange parameters $J_{i=1,2,3,4}$ as J_1 — XY interaction; J_2 — Ising interaction; J_3 — “pseudo-dipolar” interaction, and J_4 — Dzyaloshinskii-Moriya interaction. Values of $J_{i=1,2,3,4}$ for a given material can be determined from, e.g., inelastic neutron scattering experiments carried out in magnetic field^{26,28}

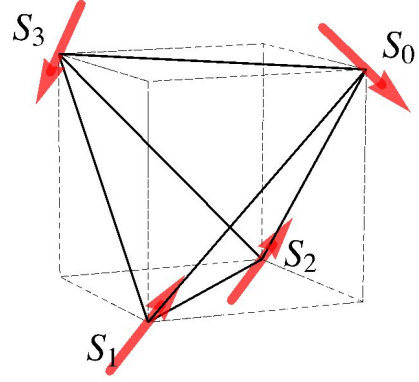


FIG. 7: A single tetrahedron within the pyrochlore lattice, showing the convention used in labelling sites. The positions of the magnetic sites relative to the centre of the tetrahedron are defined in Eq. A1.

Appendix B: Conditions for the existence of 4-sublattice order

Here we prove the assertion that the most general possible Hamiltonian for nearest-neighbour exchange interactions on the pyrochlore lattice — \mathcal{H}_{ex} [Eq. (A2)] — *always* possesses a classical ground state with vanishing crystal momentum $\mathbf{q} = 0$, and 4-sublattice long-range order.

Since \mathcal{H}_{ex} includes only nearest-neighbour bonds, all of which belong uniquely to a single tetrahedron, \mathcal{H}_{ex} can be written in terms of a sum over individual tetrahedra l

$$\mathcal{H}_{\text{ex}} = \sum_{l \in \text{A}} \mathcal{H}_{\text{ex}}^{\text{A}}[l] + \sum_{l \in \text{B}} \mathcal{H}_{\text{ex}}^{\text{B}}[l] \quad (\text{B1})$$

where A and B refer to the two distinct sublattices of tetrahedra. It follows that any state which minimises the energy of each individual tetrahedron must therefore be a ground state. Tetrahedra on the A and B sublattices are related through inversion about a single site \mathcal{I} . Since $\mathcal{I}^2 = 1$,

$$\begin{aligned} \mathbf{S}_i \cdot \mathbf{J}_{ij} \cdot \mathbf{S}_j &= \mathbf{S}_i \cdot \mathcal{I}^2 \cdot \mathbf{J}_{ij} \cdot \mathcal{I}^2 \cdot \mathbf{S}_j \\ &= \mathbf{S}_i \cdot \mathcal{I} \cdot \mathbf{J}_{ij} \cdot \mathcal{I} \cdot \mathbf{S}_j \\ \implies \mathbf{J}_{ij} &= \mathcal{I} \cdot \mathbf{J}_{ij} \cdot \mathcal{I} \end{aligned} \quad (\text{B2})$$

where we have used the fact that \mathbf{S}_i is invariant under inversion. We infer that

$$\mathcal{H}_{\text{ex}}^{\text{A}}[l] = \mathcal{H}_{\text{ex}}^{\text{B}}[l'] = \mathcal{H}_{\text{ex}}^{\text{tet}} \quad (\text{B3})$$

and the Hamiltonian for *any* tetrahedron l is the same, regardless of which sublattice it belongs to.

In the case of classical spins, $[\mathcal{H}_{\text{ex}}^{\text{A}}, \mathcal{H}_{\text{ex}}^{\text{B}}] = 0$, and we can construct a ground state of \mathcal{H}_{ex} by choosing *any* state which minimises the energy of a single tetrahedron, and repeating it across all A-sublattice (or B-sublattice) tetrahedra. The equivalence of Hamiltonians for A or

order parameter	definition in terms of spin components	associated ordered phases
m_{A_2}	$\frac{1}{2\sqrt{3}} (S_0^x + S_0^y + S_0^z + S_1^x - S_1^y - S_1^z - S_2^x + S_2^y - S_2^z - S_3^x - S_3^y + S_3^z)$	“all in-all out”
\mathbf{m}_E	$\left(\begin{array}{c} \frac{1}{2\sqrt{6}} (-2S_0^x + S_0^y + S_0^z - 2S_1^x - S_1^y - S_1^z + 2S_2^x + S_2^y - S_2^z + 2S_3^x - S_3^y + S_3^z) \\ \frac{1}{2\sqrt{2}} (-S_0^y + S_0^z + S_1^y - S_1^z - S_2^y - S_2^z + S_3^y + S_3^z) \end{array} \right)$	Ψ_2 and Ψ_3
$\mathbf{m}_{T_{1,A}}$	$\left(\begin{array}{c} \frac{1}{2}(S_0^x + S_1^x + S_2^x + S_3^x) \\ \frac{1}{2}(S_0^y + S_1^y + S_2^y + S_3^y) \\ \frac{1}{2}(S_0^z + S_1^z + S_2^z + S_3^z) \end{array} \right)$	non-collinear FM
$\mathbf{m}_{T_{1,B}}$	$\left(\begin{array}{c} \frac{-1}{2\sqrt{2}}(S_0^y + S_0^z - S_1^y - S_1^z - S_2^y + S_2^z + S_3^y - S_3^z) \\ \frac{-1}{2\sqrt{2}}(S_0^x + S_0^z - S_1^x + S_1^z - S_2^x - S_2^z + S_3^x - S_3^z) \\ \frac{-1}{2\sqrt{2}}(S_0^x + S_0^y - S_1^x + S_1^y + S_2^x - S_2^y - S_3^x - S_3^y) \end{array} \right)$	non-collinear FM
\mathbf{m}_{T_2}	$\left(\begin{array}{c} \frac{1}{2\sqrt{2}}(-S_0^y + S_0^z + S_1^y - S_1^z + S_2^y + S_2^z - S_3^y - S_3^z) \\ \frac{1}{2\sqrt{2}}(S_0^x - S_0^z - S_1^x - S_1^z - S_2^x + S_2^z + S_3^x + S_3^z) \\ \frac{1}{2\sqrt{2}}(-S_0^x + S_0^y + S_1^x + S_1^y - S_2^x - S_2^y + S_3^x - S_3^y) \end{array} \right)$	Palmer-Chalker (Ψ_4)

TABLE I: Order parameters \mathbf{m}_λ , describing how the point group symmetry of a 4-site tetrahedral unit cell, T_d , is broken by conventional magnetically-ordered phases on the pyrochlore lattice. The Ψ_i notations are taken from⁵¹.

B sublattices [Eq. (B3)] *guarantees* that all B-sublattice (or A-sublattice) will automatically have the minimum energy. Therefore there always exists a $\mathbf{q} = 0$ classical ground state with 4-sublattice long-range order, even in the presence of finite Dzyaloshinskii-Moriya interaction J_4 .

This $\mathbf{q} = 0$, 4-sublattice order is unique — up to the degeneracy of the ground state for a single tetrahedron — *provided* that the spin on every site of the tetrahedron points in a different direction in each of these ground states. Away from phase boundaries, this is true for *all* of the 4-sublattice ordered phases discussed in the main text, each of which is 6-fold degenerate. However if two of the ground states of a single tetrahedron share a common spin — i.e. the spin on a given site points in the same direction in more than one ground state — then it is *always* possible to construct other ground states with finite \mathbf{q} .

Let us suppose, for example, that two different ground states for a single tetrahedron have identical orientation of the spin on site 0, but different orientation of the spins on sites 1, 2 and 3. In this case it is possible to divide the pyrochlore lattice into a set of parallel kagome planes, containing spins associated with sites 1,2 and 3 of a tetrahedron, separated by triangular-lattice planes associated with site 0. Since each successive kagome plane can take on one of two different spin configurations, the number of such ground states grows as $2^{\mathbb{N}_K}$, where \mathbb{N}_K is the number of kagome planes, and encompasses all possible $\mathbf{q} \parallel [111]$. Dimensional reduction of this type occurring for example, on the boundary between the FM and Palmer-Chalker phases, is described below.

An even larger degeneracy occurs for the “two in, two out” states, made famous by the spin ice problem. In this case there are a total of 6 possible ground states for a single tetrahedron, but each possible spin orientation, on each site, belongs to 3 different ground states. The

total number of possible ground states on the lattice is then extensive, $\Omega_{\text{ice}} \sim (3/2)^{N/2}$, where N is the total number of sites in the lattice. This manifold of “ice” states includes ground states with all possible \mathbf{q} .

Appendix C: Symmetry classification of ordered phases

1. Definition of order parameters \mathbf{m}_λ

The symmetry operations of a tetrahedron form a 24-element group T_d , with elements: $8 \times C_3$ — $\frac{2\pi}{3}$ rotation around a [111] axis; $3 \times C_2$ — π rotation around [100] axis; $6 \times S_4$ — $\frac{\pi}{2}$ rotation around a [100] axis followed by reflection in the same [100] plane; $6 \times \sigma_d$ — reflection in [011] plane; ϵ — the identity³⁷.

It is possible to define order parameters \mathbf{m}_λ , transforming with the non-trivial irreducible representations $\lambda = \{ A_2, E, T_1, T_2 \}$ of T_d , which fully characterise all possible 4-sublattice ordered states on a pyrochlore lattice. These are listed in Table I.

The order-parameter susceptibility

$$\chi_\lambda(T) = \frac{\langle |\mathbf{m}_\lambda|^2 \rangle - \langle \mathbf{m}_\lambda \rangle^2}{T} \quad (\text{C1})$$

associated with each \mathbf{m}_λ is a useful tool for determining phase transitions in finite-temperature simulations. We note that in the case of the two, coupled T_1 order parameters, $\mathbf{m}_{T_{1,A}}$ and $\mathbf{m}_{T_{1,B}}$ (see Table I), it is convenient to group both order parameters into a single susceptibility.

2. Expression of Hamiltonian in terms of order parameters

For classical spins undergoing 4-sublattice order, the Hamiltonian \mathcal{H}_{ex} [Eq. (A2)] can be rewritten in terms of these order parameters, to give

$$\mathcal{H}_{\text{ex}}^{[\text{T}_d]} = \frac{1}{2} \left[a_{\text{A}_2} m_{\text{A}_2}^2 + a_{\text{E}} \mathbf{m}_{\text{E}}^2 + a_{\text{T}_2} \mathbf{m}_{\text{T}_2}^2 + a_{\text{T}_{1,\text{A}}} \mathbf{m}_{\text{T}_{1,\text{A}}}^2 + a_{\text{T}_{1,\text{B}}} \mathbf{m}_{\text{T}_{1,\text{B}}}^2 + a_{\text{T}_{1,\text{AB}}} \mathbf{m}_{\text{T}_{1,\text{A}}} \cdot \mathbf{m}_{\text{T}_{1,\text{B}}} \right]. \quad (\text{C2})$$

with coefficients

$$\begin{aligned} a_{\text{A}_2} &= -2J_1 + J_2 - 2(J_3 + 2J_4) \\ a_{\text{E}} &= -2J_1 + J_2 + J_3 + 2J_4 \\ a_{\text{T}_2} &= -J_2 + J_3 - 2J_4 \\ a_{\text{T}_{1,\text{A}}} &= 2J_1 + J_2 \\ a_{\text{T}_{1,\text{B}}} &= -J_2 - J_3 + 2J_4 \\ a_{\text{T}_{1,\text{AB}}} &= -\sqrt{8}J_3 \end{aligned} \quad (\text{C3})$$

For the purpose of finding the ground states, the Hamiltonian $\mathcal{H}_{\text{ex}}^{[\text{T}_d]}$ can be reduced to a form quadratic in \mathbf{m}_λ by a coordinate transformation

$$\begin{aligned} \mathbf{m}_{\text{T}_{1,\text{A}'}} &= \cos \theta_{\text{T}_1} \mathbf{m}_{\text{T}_{1,\text{A}}} - \sin \theta_{\text{T}_1} \mathbf{m}_{\text{T}_{1,\text{B}}} \\ \mathbf{m}_{\text{T}_{1,\text{B}'}} &= \sin \theta_{\text{T}_1} \mathbf{m}_{\text{T}_{1,\text{A}}} + \cos \theta_{\text{T}_1} \mathbf{m}_{\text{T}_{1,\text{B}}} \end{aligned} \quad (\text{C4})$$

where

$$\theta_{\text{T}_1} = \frac{1}{2} \arctan \left(\frac{\sqrt{8}J_3}{2J_1 + 2J_2 + J_3 - 2J_4} \right). \quad (\text{C5})$$

is the canting angle between spins and the relevant [100] axis. The Hamiltonian then becomes

$$\mathcal{H}_{\text{ex}}^{[\text{T}_d]} = \frac{1}{2} \left[a_{\text{A}_2} m_{\text{A}_2}^2 + a_{\text{E}} \mathbf{m}_{\text{E}}^2 + a_{\text{T}_2} \mathbf{m}_{\text{T}_2}^2 + a_{\text{T}_{1,\text{A}'}} \mathbf{m}_{\text{T}_{1,\text{A}'}}^2 + a_{\text{T}_{1,\text{B}'}} \mathbf{m}_{\text{T}_{1,\text{B}'}}^2 \right]. \quad (\text{C6})$$

with coefficients given in Table II.

The minimisation of the energy is always subjected to the constraint that every spin has fixed length $S^2 = 1/4$. It is convenient to express this as

$$\begin{aligned} \mathbf{S}_0^2 + \mathbf{S}_1^2 + \mathbf{S}_2^2 + \mathbf{S}_3^2 &= 1 \\ \mathbf{S}_0^2 + \mathbf{S}_1^2 - \mathbf{S}_2^2 - \mathbf{S}_3^2 &= 0 \\ \mathbf{S}_0^2 - \mathbf{S}_1^2 + \mathbf{S}_2^2 - \mathbf{S}_3^2 &= 0 \\ \mathbf{S}_0^2 - \mathbf{S}_1^2 - \mathbf{S}_2^2 + \mathbf{S}_3^2 &= 0 \end{aligned} \quad (\text{C7})$$

for our further calculation. We note that the addition of single-ion anisotropy only changes the coefficient a_λ in equation (C6) and so could be easily included in our analysis.

coefficient of $ \mathbf{m}_\lambda ^2$	definition in terms of exchange parameters
a_{A_2}	$-2J_1 + J_2 - 2(J_3 + 2J_4)$
a_{E}	$-2J_1 + J_2 + J_3 + 2J_4$
a_{T_2}	$-J_2 + J_3 - 2J_4$
$a_{\text{T}_{1,\text{A}'}}$	$(2J_1 + J_2) \cos^2(\theta_{\text{T}_1}) - (J_2 + J_3 - 2J_4) \sin^2(\theta_{\text{T}_1}) + \sqrt{2}J_3 \sin(2\theta_{\text{T}_1})$
$a_{\text{T}_{1,\text{B}'}}$	$(2J_1 + J_2) \sin^2(\theta_{\text{T}_1}) - (J_2 + J_3 - 2J_4) \cos^2(\theta_{\text{T}_1}) - \sqrt{2}J_3 \sin(2\theta_{\text{T}_1})$

TABLE II: Coefficients a_λ of the scalar invariants $|\mathbf{m}_\lambda|^2$ appearing in $\mathcal{H}'_{\text{ex}}^{[\text{T}_d]}$ [Eq. (C6)]. The classical ground states of \mathcal{H}_{ex} [Eq. (A2)] for a given set of parameters (J_1, J_2, J_3, J_4) can be found by identifying the coefficient(s) a_λ with the lowest value, and imposing the constraint Eq. (C7) on the associated \mathbf{m}_λ . The canting angle θ_{T_1} is defined in Eq. (C5).

3. Phases and phase transitions predicted by $\mathcal{H}'_{\text{ex}}^{[\text{T}_d]}$

The Hamiltonian $\mathcal{H}'_{\text{ex}}^{[\text{T}_d]}$ [Eq. (C6)] leads very directly to a classical ground state phase diagram. The sum of the squares of the order parameters are constrained via Eq. (C7)

$$m_{\text{A}_2}^2 + \mathbf{m}_{\text{E}}^2 + \mathbf{m}_{\text{T}_2}^2 + \mathbf{m}_{\text{T}_{1,\text{A}'}}^2 + \mathbf{m}_{\text{T}_{1,\text{B}'}}^2 \equiv \sum_{\lambda} m_{\lambda}^2 = 1, \quad (\text{C8})$$

and each individual order parameter is constructed to have a maximal magnitude of unity

$$\max \mathbf{m}_\lambda^2 = 1. \quad (\text{C9})$$

Taken together, these facts imply that the classical ground state of \mathcal{H}_{ex} [Eq. (A2)] can be found by first identifying the coefficient a_λ of $\mathcal{H}'_{\text{ex}}^{[\text{T}_d]}$ [Eq. (C2)] with the minimum value, and then imposing the constraint Eq. (C7) on \mathbf{m}_λ .

For $J_3 < 0$ and $J_4 \equiv 0$, the coefficients a_λ with the lowest values can be a_{E} , $a_{\text{T}_{1,\text{A}'}}$, and a_{T_2} , depending on the values of J_1 and J_2 , and the ground states found have E, T_1 and T_2 symmetry. The boundaries between these phases occur where $a_{\text{T}_2} = a_{\text{E}}$, $a_{\text{T}_2} = a_{\text{T}_{1,\text{A}'}}$, and $a_{\text{E}} = a_{\text{T}_{1,\text{A}'}}$. In the present case, these expressions reduce to

$$a_{\text{T}_2} = a_{\text{E}} < a_{\text{T}_2}, a_{\text{T}_{1,\text{B}'}} , a_{\text{A}_2} \Rightarrow J_2 = J_1 > 0 \quad (\text{C10})$$

$$a_{\text{T}_2} = a_{\text{T}_{1,\text{A}'}} < a_{\text{E}}, a_{\text{T}_{1,\text{B}'}} , a_{\text{A}_2} \Rightarrow J_2 = -J_1 > 0 \quad (\text{C11})$$

$$a_{\text{E}} = a_{\text{T}_{1,\text{A}'}} < a_{\text{T}_2}, a_{\text{T}_{1,\text{B}'}} , a_{\text{A}_2} \Rightarrow J_2 = \frac{J_1(4J_1 - 5J_3)}{4J_1 - J_3} < 0 \quad (\text{C12})$$

where θ_{T_1} is defined in Eq. (C5). The regions bounded by these curves are shown in Fig. 8.

On the boundaries between phases with different symmetry, the set of possible ground states include states with finite values of *both* order parameters, subject to the constraint Eq. (C7). The three distinct $T = 0$ ground states for $J_3 < 0$ and $J_4 \equiv 0$, and the associated phase boundaries, are discussed in detail below.

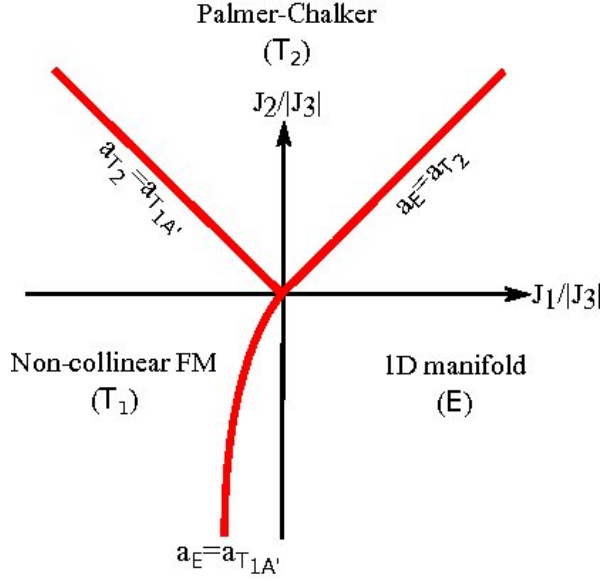


FIG. 8: Classical ground state phase diagram of \mathcal{H}_{ex} [Eq. (A2)] for $J_3 < 0$, $J_4 = 0$, as a function of $(J_1, J_2)/|J_3|$. In the absence of fluctuations, the ground states are a non-collinear FM transforming with the T_1 irrep of T_d ; a one-dimensional manifold of states transforming with the E irrep of T_d ; and the Palmer-Chalker phase, a coplanar antiferromagnet transforming with the T_2 irrep of T_d . All three phases have long-range 4-sublattice order. Analytical expressions for the boundaries between phases are given in Eq. (C10–C12), with coefficients a_λ defined in Table II.

Appendix D: 4-sublattice ordered states for $J_3 < 0$, $J_4 \equiv 0$.

Non-collinear FM with T_1 symmetry

In a region bounded by $a_{T_{1A'}} = a_{T_2}$ [Eq. (C11)] , and $a_{T_{1A'}} = a_E$ [Eq. (C12)] — cf. Fig. 8 — the energy is

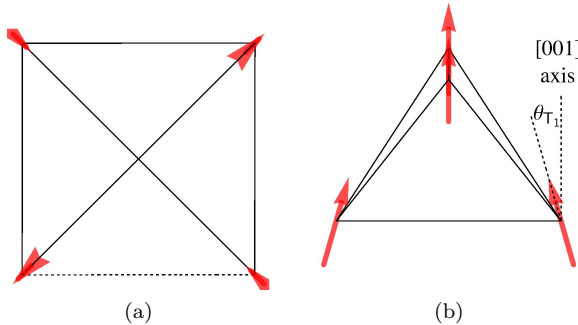


FIG. 9: Spin-configuration in the 4-sublattice non-collinear FM phase : (a) viewed along the [001] axis; (b) viewed slightly off the [110] axis. The magnetisation is aligned with the [001] axis. Spins are canted into the plane perpendicular to this, with canting angle θ_{T_1} , in an “ice-like” manner.

minimised by setting

$$\mathbf{m}_{T_{1A'}}^2 = 1 \quad (\text{D1})$$

and

$$m_{A_2} = \mathbf{m}_E = \mathbf{m}_{T_2} = \mathbf{m}_{T_{1B'}} = 0 \quad (\text{D2})$$

The constraints on the total length of the spin, Eq. (C7) further imply that

$$\begin{aligned} m_{T_{1A'}}^y m_{T_{1A'}}^z &= 0 \\ m_{T_{1A'}}^x m_{T_{1A'}}^z &= 0 \\ m_{T_{1A'}}^x m_{T_{1A'}}^y &= 0. \end{aligned} \quad (\text{D3})$$

It follows that there are 6 possible ground states

$$\mathbf{m}_{T_{1A'}} = \begin{pmatrix} \pm 1 \\ 0 \\ 0 \end{pmatrix}, \begin{pmatrix} 0 \\ \pm 1 \\ 0 \end{pmatrix}, \begin{pmatrix} 0 \\ 0 \\ \pm 1 \end{pmatrix}. \quad (\text{D4})$$

Written in terms of spins, these are 6, non-collinear ferromagnetic (FM) ground states, with typical spin configuration

$$\begin{aligned} \mathbf{S}_0 &= S \left(\sin \theta_{T_1}/\sqrt{2}, \sin \theta_{T_1}/\sqrt{2}, \cos \theta_{T_1} \right) \\ \mathbf{S}_1 &= S \left(-\sin \theta_{T_1}/\sqrt{2}, \sin \theta_{T_1}/\sqrt{2}, \cos \theta_{T_1} \right) \\ \mathbf{S}_2 &= S \left(\sin \theta_{T_1}/\sqrt{2}, -\sin \theta_{T_1}/\sqrt{2}, \cos \theta_{T_1} \right) \\ \mathbf{S}_3 &= S \left(-\sin \theta_{T_1}/\sqrt{2}, -\sin \theta_{T_1}/\sqrt{2}, \cos \theta_{T_1} \right) \end{aligned} \quad (\text{D5})$$

where θ_{T_1} is given by Eq. (C5).

The magnetisation of this FM ground state, illustrated in Fig. 9, is parallel to a [001] axis, with spins canted away from this axis, in an “ice-like” manner. This state has been identified as the ground state in $\text{Yb}_2\text{Sn}_2\text{O}_7$, where it was referred to as a “splayed FM” [39], and in those samples of $\text{Yb}_2\text{Ti}_2\text{O}_7$ which order at low temperature⁴⁸.

One-dimensional manifold of states with E symmetry

In a region bounded by $a_E = a_{T_{1A'}}$ [Eq. (C12)] and $a_E = a_{T_2}$ [Eq. (C10)] — cf. Fig. 8 — the energy is minimised by setting

$$\mathbf{m}_E^2 = 1 \quad (\text{D6})$$

and

$$m_{A_2} = \mathbf{m}_{T_2} = \mathbf{m}_{T_{1A'}} = \mathbf{m}_{T_{1B'}}. \quad (\text{D7})$$

These solutions *automatically* satisfy the constraint on the total length of the spin Eq. (C7), and are conveniently characterised by writing

$$\mathbf{m}_E = (\cos \theta_E, \sin \theta_E) \quad (\text{D8})$$

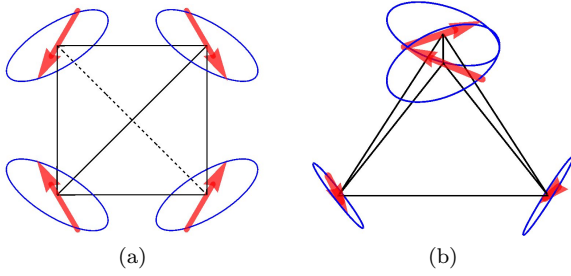


FIG. 10: Example of a spin configuration within the one-dimensional manifold of states transforming with the \mathbf{E} irrep of \mathbf{T}_d : (a) viewed along $[001]$ axis; (b) viewed slightly off the $[110]$ axis. The manifold possesses 4-sublattice long-range order, with spins lying in the “ XY ” plane perpendicular to the local $[111]$ axis at each site. The manifold is continuous, and can be parameterised with a single angle $\theta_{\mathbf{E}}$.

It follows that the ground state is a continuous, one-dimensional manifold of states parameterised by the single angle $0 \leq \theta_{\mathbf{E}} < 2\pi$. The spin configuration in this manifold is given by

$$\begin{aligned}
 \mathbf{S}_0 &= S \left(\sqrt{\frac{2}{3}} \cos(\theta_{\mathbf{E}}), \sqrt{\frac{2}{3}} \cos(\theta_{\mathbf{E}} + \frac{2\pi}{3}), \right. \\
 &\quad \left. \sqrt{\frac{2}{3}} \cos(\theta_{\mathbf{E}} - \frac{2\pi}{3}) \right) \\
 \mathbf{S}_1 &= S \left(\sqrt{\frac{2}{3}} \cos(\theta_{\mathbf{E}}), -\sqrt{\frac{2}{3}} \cos(\theta_{\mathbf{E}} + \frac{2\pi}{3}), \right. \\
 &\quad \left. -\sqrt{\frac{2}{3}} \cos(\theta_{\mathbf{E}} - \frac{2\pi}{3}) \right) \\
 \mathbf{S}_2 &= S \left(-\sqrt{\frac{2}{3}} \cos(\theta_{\mathbf{E}}), \sqrt{\frac{2}{3}} \cos(\theta_{\mathbf{E}} + \frac{2\pi}{3}), \right. \\
 &\quad \left. -\sqrt{\frac{2}{3}} \cos(\theta_{\mathbf{E}} - \frac{2\pi}{3}) \right) \\
 \mathbf{S}_3 &= S \left(-\sqrt{\frac{2}{3}} \cos(\theta_{\mathbf{E}}), -\sqrt{\frac{2}{3}} \cos(\theta_{\mathbf{E}} + \frac{2\pi}{3}), \right. \\
 &\quad \left. \sqrt{\frac{2}{3}} \cos(\theta_{\mathbf{E}} - \frac{2\pi}{3}) \right). \tag{D9}
 \end{aligned}$$

Within this one-dimensional manifold of states, each spin \mathbf{S}_i lies in the local “ XY ” plane normal to $\hat{\mathbf{r}}_i$ [cf Eq. (A1)].

Non-coplanar antiferromagnet, Ψ_2 , with \mathbf{E} symmetry

For parameters bordering on the Palmer-Chalker phase [cf Fig. 1, main text], fluctuations select a non-coplanar antiferromagnet, Ψ_2 , from the one-dimensional manifold of states transforming with \mathbf{E} . The Ψ_2 ground state is six-fold degenerate, with spins canted symmetrically out of the $[100]$ plane.

The six spin configurations for Ψ_2 states are given by Eq. (D9) with $\theta_{\mathbf{E}} = \frac{n\pi}{3}$, $n = 0, 1, 2 \dots 5$. The Ψ_2 state is

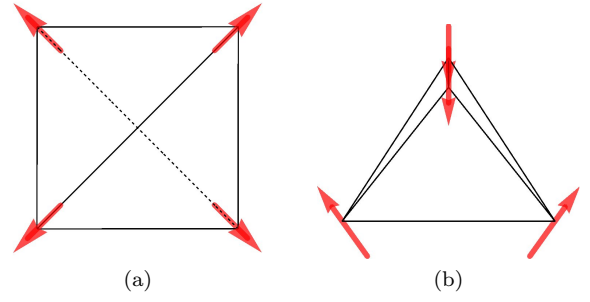


FIG. 11: Spin configuration in the 4-sublattice non-coplanar antiferromagnet, Ψ_2 , selected by fluctuations from the one-dimensional manifold of states transforming with \mathbf{E} : (a) viewed along $[001]$ axis; (b) viewed slightly off the $[110]$ axis. At the phase boundary with the Palmer-Chalker phase, each of the six Ψ_2 ground states can be transformed continuously into a Palmer-Chalker state.

characterised by the primary order parameter $\mathbf{m}_{\mathbf{E}}$ [cf. Table I], and by $c_{\mathbf{E}} > 0$, where

$$c_{\mathbf{E}} = \langle \cos 6\theta_{\mathbf{E}} \rangle \tag{D10}$$

An example of a typical spin configuration is shown in Fig. (11).

Coplanar antiferromagnet, Ψ_3 , with \mathbf{E} symmetry

For parameters bordering on the non-collinear FM phase, fluctuations select a coplanar antiferromagnet, Ψ_3 , from the one-dimensional manifold of states transforming with \mathbf{E} . The Ψ_3 ground state is six-fold degenerate, with spins lying in a common $[100]$ plane.

The six spin configurations for Ψ_3 states are given by Eq. (D9) with $\theta = \frac{(2n+1)\pi}{6}$, $n = 0, 1, 2 \dots 5$. These states are characterised by a finite value of the order parameter $\mathbf{m}_{\mathbf{E}}$ [cf Table I], and by $c_{\mathbf{E}} < 0$ [cf. Eq. (D10)]. An example of a typical spin configuration is shown in Fig. (12).

Taken together Ψ_2 and Ψ_3 form a complete basis for the \mathbf{E} irrep of \mathbf{T}_d .

Palmer-Chalker phase [Ψ_4] with \mathbf{T}_2 symmetry

In a region bounded by $a_{\mathbf{T}_2} = a_{\mathbf{T}_{1A'}}$ [Eq. (C11)] and $a_{\mathbf{T}_2} = a_{\mathbf{E}}$ [Eq. (C10)] — cf. Fig. 8 — the energy is minimised by setting

$$\mathbf{m}_{\mathbf{T}_2}^2 = 1 \tag{D11}$$

and

$$m_{A_2} = \mathbf{m}_{\mathbf{E}} = \mathbf{m}_{\mathbf{T}_{1A'}} = \mathbf{m}_{\mathbf{T}_{1B'}} = 0 \tag{D12}$$

The constraints on the total length of the spin,

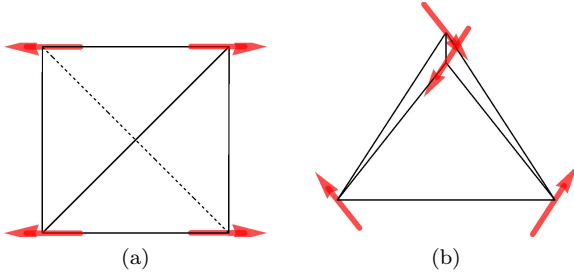


FIG. 12: Spin configuration in the 4-sublattice coplanar antiferromagnet, Ψ_3 , selected by fluctuations from the one-dimensional manifold of states transforming with \mathbf{E} : (a) viewed along $[001]$ axis; (b) viewed slightly off the $[110]$ axis. At the phase boundary with the non-collinear FM phase, each of the six Ψ_3 ground states can be transformed continuously into a non-collinear FM state.

Eq. (C7) further imply that

$$\mathbf{m}_{\mathbf{T}_2}^2 = 1 \quad (\text{D13})$$

$$m_{\mathbf{T}_2}^y m_{\mathbf{T}_2}^z = 0 \quad (\text{D14})$$

$$m_{\mathbf{T}_2}^x m_{\mathbf{T}_2}^z = 0 \quad (\text{D15})$$

$$m_{\mathbf{T}_2}^x m_{\mathbf{T}_2}^y = 0 \quad (\text{D16})$$

giving us a set of 6 ground states

$$\mathbf{m}_{\mathbf{T}_2} = \begin{pmatrix} \pm 1 \\ 0 \\ 0 \end{pmatrix}, \begin{pmatrix} 0 \\ \pm 1 \\ 0 \end{pmatrix}, \begin{pmatrix} 0 \\ 0 \\ \pm 1 \end{pmatrix}. \quad (\text{D17})$$

Within these ground states spins are arranged in helical manner in a common $[100]$ plane, with a typical spin configuration given by (see Fig. 13).

$$\begin{aligned} \mathbf{S}_0 &= S(\sqrt{2}/2, -\sqrt{2}/2, 0) \\ \mathbf{S}_1 &= S(-\sqrt{2}/2, -\sqrt{2}/2, 0) \\ \mathbf{S}_2 &= S(\sqrt{2}/2, \sqrt{2}/2, 0) \\ \mathbf{S}_3 &= S(-\sqrt{2}/2, \sqrt{2}/2, 0) \end{aligned} \quad (\text{D18})$$

This phase is the ‘‘Palmer-Chalker’’ phase, first identified as the ground state of a model with antiferromagnetic nearest neighbour Heisenberg interactions and long range dipolar interactions on the pyrochlore lattice³⁸.

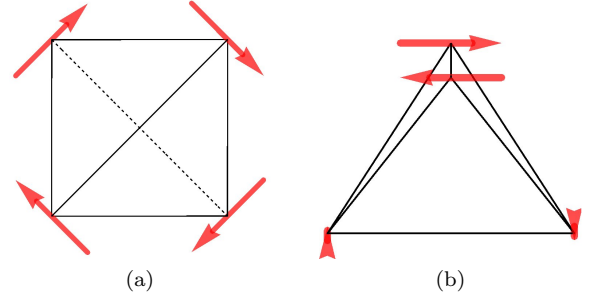


FIG. 13: Spin configuration in the 4-sublattice Palmer-Chalker phase, Ψ_4 , transforming with the \mathbf{T}_2 irrep of \mathbf{T}_d : (a) viewed along $[001]$ axis; (b) viewed slightly off the $[110]$ axis. At the phase boundary with the Ψ_2 phase, each of the six Palmer-Chalker ground states can be transformed continuously into a Ψ_2 state.

Appendix E: Ground-state degeneracy on classical phase boundaries

1. Boundary between Palmer-Chalker phase and the one-dimensional manifold of states with \mathbf{E} symmetry

The boundary between the Palmer-Chalker phase and the one-dimensional manifold of states with \mathbf{E} symmetry occurs when $a_{\mathbf{E}} = a_{\mathbf{T}_2}$ [cf. Eq. (C10)]. In this case, $\mathcal{H}'_{\text{ex}}^{[\mathbf{T}_d]}$ [Eq. (C6)] is minimised by setting

$$\mathbf{m}_{\mathbf{E}}^2 + \mathbf{m}_{\mathbf{T}_2}^2 = 1 \quad (\text{E1})$$

and

$$m_{\mathbf{A}_2} = \mathbf{m}_{\mathbf{T}_{1A'}} = \mathbf{m}_{\mathbf{T}_{1B'}} = 0. \quad (\text{E2})$$

Substituting from Eq. (D8), and imposing the constraint Eq. (C7), we find

$$\begin{aligned} 2m_{\mathbf{E}}m_{\mathbf{T}_2}^x \sin(\theta_{\mathbf{E}}) - m_{\mathbf{T}_2}^y m_{\mathbf{T}_2}^z &= 0 \\ 2m_{\mathbf{E}}m_{\mathbf{T}_2}^y \sin\left(\theta_{\mathbf{E}} - \frac{2\pi}{3}\right) - m_{\mathbf{T}_2}^x m_{\mathbf{T}_2}^z &= 0 \\ 2m_{\mathbf{E}}m_{\mathbf{T}_2}^z \sin\left(\theta_{\mathbf{E}} + \frac{2\pi}{3}\right) - m_{\mathbf{T}_2}^x m_{\mathbf{T}_2}^y &= 0. \end{aligned} \quad (\text{E3})$$

It is easy to show that there are no solutions to Eqs. (E3) where more than one component of $\mathbf{m}_{\mathbf{T}_2}$ is finite. There are, however, three distinct one-dimensional manifolds which connect pairs of Palmer-Chalker states

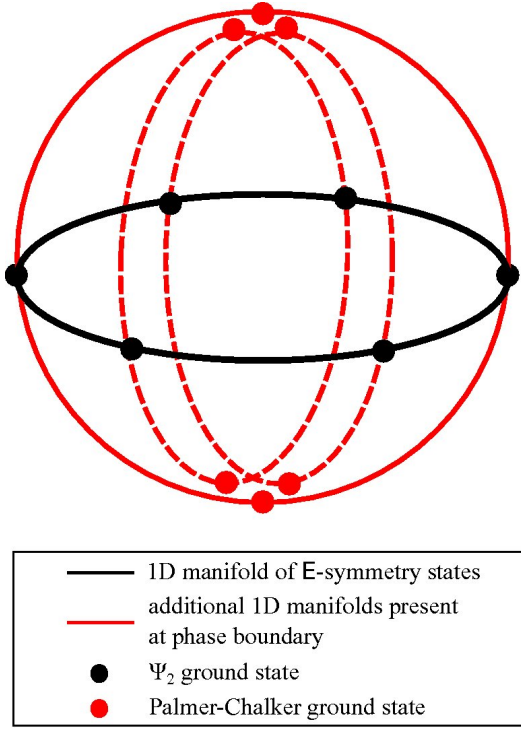


FIG. 14: Structure of the ground state manifold at the boundary between the Palmer-Chalker (PC) phase and the one-dimensional manifold of states with E symmetry. The black circle denotes the manifold of E-symmetry ground states, including the six Ψ_2 ground states (black dots). At the boundary with the PC phase, this manifold branches at the Ψ_2 states, to connect with three, additional, one-dimensional manifolds. These manifolds in turn interpolate to the six Palmer-Chalker ground states with T_2 symmetry (red dots). An exactly equivalent picture holds on the boundary between the non-collinear ferromagnet (FM), and the one-dimensional manifold of states with E symmetry. However in this case the different manifolds intersect at the Ψ_3 states.

to the one-dimensional manifold of E-symmetry states:

$$\mathbf{m}_E = \cos(\alpha) \begin{pmatrix} 1 \\ 0 \end{pmatrix}, \quad \mathbf{m}_{T_2} = \sin(\alpha) \begin{pmatrix} 0 \\ 0 \end{pmatrix} \quad (\text{E4})$$

$$\mathbf{m}_E = \cos(\beta) \begin{pmatrix} -\frac{1}{2} \\ \frac{\sqrt{3}}{2} \end{pmatrix}, \quad \mathbf{m}_{T_2} = \sin(\beta) \begin{pmatrix} 0 \\ 1 \\ 0 \end{pmatrix} \quad (\text{E5})$$

$$\mathbf{m}_E = \cos(\gamma) \begin{pmatrix} -\frac{1}{2} \\ -\frac{\sqrt{3}}{2} \end{pmatrix}, \quad \mathbf{m}_{T_2} = \sin(\gamma) \begin{pmatrix} 0 \\ 0 \\ 1 \end{pmatrix} \quad (\text{E6})$$

where the angles α , β and γ run from 0 to 2π .

A typical spin configuration for one of the three con-

necting manifolds is

$$\begin{aligned} \mathbf{S}_0 &= S\sqrt{\frac{2}{3}} \left(-\cos(\alpha), \cos\left(\alpha + \frac{\pi}{3}\right), \cos\left(\alpha - \frac{\pi}{3}\right) \right) \\ \mathbf{S}_1 &= S\sqrt{\frac{2}{3}} \left(-\cos(\alpha), -\cos\left(\alpha + \frac{\pi}{3}\right), -\cos\left(\alpha - \frac{\pi}{3}\right) \right) \\ \mathbf{S}_2 &= S\sqrt{\frac{2}{3}} \left(\cos(\alpha), \cos\left(\alpha - \frac{\pi}{3}\right), -\cos\left(\alpha + \frac{\pi}{3}\right) \right), \\ \mathbf{S}_3 &= S\sqrt{\frac{2}{3}} \left(\cos(\alpha), -\cos\left(\alpha - \frac{\pi}{3}\right), \cos\left(\alpha + \frac{\pi}{3}\right) \right) \end{aligned} \quad (\text{E7})$$

where $\alpha = 0$ corresponds to the Ψ_2 ground state with $\theta_E = 0$, and $\alpha = \pi/2$ to one of the six Palmer-Chalker ground states. These manifolds are illustrated in Fig. 14.

2. Boundary between the non-collinear ferromagnet and the one-dimensional manifold of states with E symmetry

The boundary between the Palmer-Chalker phase and the one-dimensional manifold of states with E symmetry occurs when $a_E = a_{T_{1,A'}}$ [cf. Eq. (C12)]. In this case, $\mathcal{H}'_{\text{ex}}^{[T_d]}$ [Eq. (C6)] is minimised by setting

$$\mathbf{m}_{T_{1,A'}}^2 + \mathbf{m}_E^2 = 1 \quad (\text{E8})$$

and

$$m_{A_2} = \mathbf{m}_{T_{1,B'}} = \mathbf{m}_{T_2} = 0. \quad (\text{E9})$$

Imposing the constraint Eq. C7 we obtain

$$\begin{aligned} 2m_E m_{T_1}^x \cos(\theta_E) &= -\frac{\mu(\theta_{T_1})}{\nu(\theta_{T_1})} m_{T_{1,B'}}^y m_{T_{1,B'}}^z \\ 2m_E m_{T_1}^y \cos\left(\theta_E - \frac{2\pi}{3}\right) &= -\frac{\mu(\theta_{T_1})}{\nu(\theta_{T_1})} m_{T_{1,B'}}^x m_{T_{1,B'}}^z \\ 2m_E m_{T_1}^z \cos\left(\theta_E + \frac{2\pi}{3}\right) &= -\frac{\mu(\theta_{T_1})}{\nu(\theta_{T_1})} m_{T_{1,B'}}^x m_{T_{1,B'}}^y \end{aligned} \quad (\text{E10})$$

where θ_{FM} is the (fixed) canting angle [Eq. (C5)], θ_E is the (variable) angle within the U(1) manifold [Eq. (D8)]. For the parameters considered here, μ and ν are always finite and are given by

$$\begin{aligned} \mu(\theta_{T_1}) &= (\sqrt{2} \cos(\theta_{T_1}) - \sin(\theta_{T_1})) \\ \nu(\theta_{T_1}) &= (\sin(\theta_{T_1})^2 + \sqrt{2} \sin(2\theta_{T_1})) \end{aligned} \quad (\text{E11})$$

Arguments identical to those developed for the boundary with the Palmer-Chalker phase, give us three further 1D manifolds addition to that associated with the E phase. However the intersections of the manifolds are now located at $\theta_E = \frac{2(n+1)\pi}{6}$, corresponding to the Ψ_3 states. This explaining the model's general entropic preference for Ψ_3 states in the region proximate to the ferromagnetic phase.

A typical spin configuration for one of the three connecting manifolds, parameterised by an angle η is

$$\begin{aligned}
\mathbf{S}_0 &= S \left(\cos(\theta_{\tau_1}) \sin(\eta), \frac{1}{\sqrt{2}}(-\cos(\eta) + \sin(\eta) \sin(\theta_{\tau_1})), \right. \\
&\quad \left. \frac{1}{\sqrt{2}}(\cos(\eta) + \sin(\eta) \sin(\theta_{\tau_1})) \right) \\
\mathbf{S}_1 &= S \left(\cos(\theta_{\tau_1}) \sin(\eta), \frac{1}{\sqrt{2}}(\cos(\eta) - \sin(\eta) \sin(\theta_{\tau_1})), \right. \\
&\quad \left. \frac{1}{\sqrt{2}}(-\cos(\eta) - \sin(\eta) \sin(\theta_{\tau_1})) \right) \\
\mathbf{S}_2 &= S \left(\cos(\theta_{\tau_1}) \sin(\eta), \frac{1}{\sqrt{2}}(-\cos(\eta) - \sin(\eta) \sin(\theta_{\tau_1})), \right. \\
&\quad \left. \frac{1}{\sqrt{2}}(-\cos(\eta) + \sin(\eta) \sin(\theta_{\tau_1})) \right) \\
\mathbf{S}_3 &= S \left(\cos(\theta_{\tau_1}) \sin(\eta), \frac{1}{\sqrt{2}}(\cos(\eta) + \sin(\eta) \sin(\theta_{\tau_1})), \right. \\
&\quad \left. \frac{1}{\sqrt{2}}(\cos(\eta) - \sin(\eta) \sin(\theta_{\tau_1})) \right). \tag{E12}
\end{aligned}$$

Here $\eta = 0$ corresponds to the Ψ_3 ground state with $\theta_E = \pi/2$, and $\eta = \pi/2$ to one of the six FM ground states.

3. Boundary between the Palmer-Chalker phase and non-collinear ferromagnet

The boundary between the Palmer-Chalker phase and the non-collinear ferromagnet occurs when $a_{\tau_2} = a_{\tau_{1A'}}$ [cf. Eq. (C11)]. In this case, $\mathcal{H}'_{\text{ex}}[\Gamma_d]$ [Eq. (C6)] is minimised by setting

$$\mathbf{m}_{\tau_2}^2 + \mathbf{m}_{\tau_{1A'}}^2 = 1 \tag{E13}$$

and

$$m_{A_2} = \mathbf{m}_E = \mathbf{m}_{\tau_{1B'}} = 0. \tag{E14}$$

Imposing the constraint Eq. C7 we obtain

$$\begin{aligned}
&-m_{\tau_2}^y m_{\tau_2}^z + (\sin(\theta_{\tau_1})^2 + \sqrt{2} \sin(2\theta_{\tau_1})) m_{\tau_{1A'}}^y m_{\tau_{1A'}}^z \\
&\quad + (\sqrt{2} \cos(\theta_{\tau_1}) - \sin(\theta_{\tau_1})) (\mathbf{m}_{\tau_{1A'}} \times \mathbf{m}_{\tau_2})_x = 0 \\
&-m_{\tau_2}^x m_{\tau_2}^z + (\sin(\theta_{\tau_1})^2 + \sqrt{2} \sin(2\theta_{\tau_1})) m_{\tau_{1A'}}^x m_{\tau_{1A'}}^z \\
&\quad + (\sqrt{2} \cos(\theta_{\tau_1}) - \sin(\theta_{\tau_1})) (\mathbf{m}_{\tau_{1A'}} \times \mathbf{m}_{\tau_2})_y = 0 \\
&-m_{\tau_2}^x m_{\tau_2}^y + (\sin(\theta_{\tau_1})^2 + \sqrt{2} \sin(2\theta_{\tau_1})) m_{\tau_{1A'}}^x m_{\tau_{1A'}}^y \\
&\quad + (\sqrt{2} \cos(\theta_{\tau_1}) - \sin(\theta_{\tau_1})) (\mathbf{m}_{\tau_{1A'}} \times \mathbf{m}_{\tau_2})_z = 0
\end{aligned} \tag{E15}$$

where θ_{τ_1} is defined in Eq. (C5).

In general, the ground state manifold on the boundary of the Palmer-Chalker phase is two-dimensional. To

establish this, we consider small deviations from a given solution

$$\begin{aligned}
\mathbf{m}_{\tau_2} &= \mathbf{m}_{\tau_2}^0 + \delta \mathbf{m}_{\tau_2} \\
\mathbf{m}_{\tau_{1A'}} &= \mathbf{m}_{\tau_{1A'}}^0 + \delta \mathbf{m}_{\tau_{1A'}}
\end{aligned} \tag{E16}$$

and expand the constraint Eq. (E15) to linear order in $\delta \mathbf{m}$. Generally, we find two linearly-independent solutions for $(\delta \mathbf{m}_{\tau_2}, \delta \mathbf{m}_{\tau_{1A'}})$, and the manifold in the vicinity of $(\mathbf{m}_{\tau_2}^0, \mathbf{m}_{\tau_{1A'}}^0)$ is locally two-dimensional.

However if we expand around a state $(\tilde{\mathbf{m}}_{\tau_2}^0, \tilde{\mathbf{m}}_{\tau_{1A'}}^0)$ where *both* order parameters are aligned with the same cubic axis, e.g.

$$\tilde{m}_{\tau_2}^{0y} = \tilde{m}_{\tau_2}^{0z} = \tilde{m}_{\tau_{1A'}}^{0y} = \tilde{m}_{\tau_{1A'}}^{0z} = 0 \tag{E17}$$

one of the Eqs. (E15) is satisfied trivially, leaving only three constraints on six variables. It follows that the manifold is locally three-dimensional in the vicinity of $(\tilde{\mathbf{m}}_{\tau_2}^0, \tilde{\mathbf{m}}_{\tau_{1A'}}^0)$.

On a final note, the emergent degeneracies observed in presence of inverse Dzyaloshinskii-Moriya interactions^{52,53} can be described in the same way when turning J_4 positive.

Appendix F: Classical low-temperature expansion

We have performed a classical, low-temperature (low-T) spin-wave expansion around each of the three different ordered phases identified in the main text. This has a number of applications. Firstly, by calculating the entropy associated with each of the E symmetry states, we can determine the phase boundary between the Ψ_2 and Ψ_3 ground states in the limit $T \rightarrow 0$ [cf. Fig. 1, main text]. Secondly, knowledge of the spin wave dispersion provides further insight into the nature of the degeneracies where phases with different symmetries meet. And thirdly, by using the low-T expansion to calculate the structure factor $S(\mathbf{q})$, we can link correlation functions measured in experiment explicitly to the (classical) spin-wave spectrum. Finally, the low-T expansion also provides a useful benchmark for classical Monte Carlo simulations, particularly at low temperatures, where simulations are hard to equilibrate.

We define a local co-ordinate system by introducing a set of orthogonal unit vectors $\{\mathbf{u}_i, \mathbf{v}_i, \mathbf{w}_i\}$ for each of the four sublattices $i = 0, 1, 2, 3$ [cf. Fig. 7]. The local “z-axis”, \mathbf{w}_i , is chosen to be aligned with the spins in a given four-sublattice ground state

$$\mathbf{S}_i = S \mathbf{w}_i \quad \forall i \tag{F1}$$

The remaining unit vectors, \mathbf{u}_i and \mathbf{v}_i , are only determined up to a rotation about \mathbf{w}_i , and any convenient choice can be made.

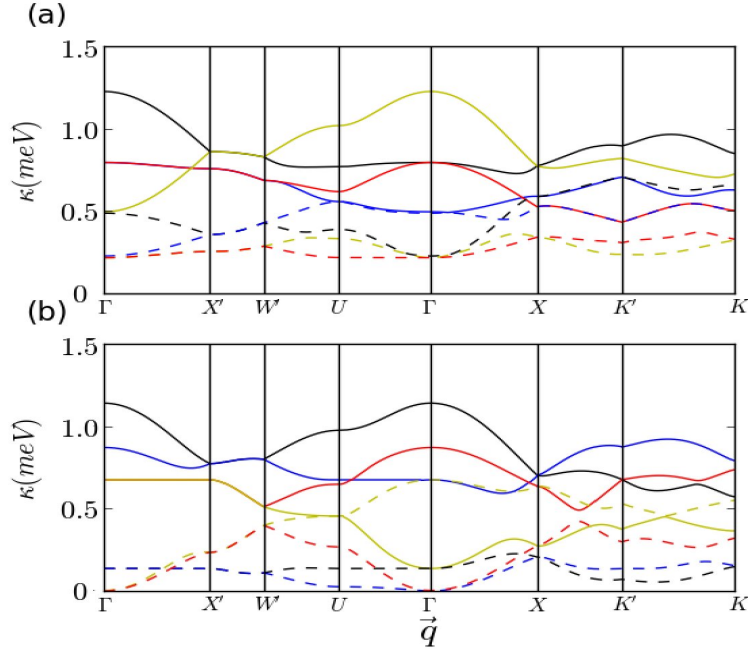


FIG. 15: Spin-wave dispersion calculated within a classical, low-temperature expansion, showing dimensional reduction of a subset of excitations. (a) Excitations of the FM ground state, for exchange parameters appropriate to $\text{Yb}_2\text{Ti}_2\text{O}_7$, i.e. $J_1 = -0.09\text{meV}$, $J_2 = -0.22\text{meV}$, $J_3 = -0.29\text{meV}$, setting $J_4 = 0$. The ferromagnet possesses a flat band in the (h, h, h) ($\Gamma \rightarrow U$) direction at energy $\Delta = 0.22\text{meV}$, which gives rise to rods in the equal time structure factor (cf. Fig. 5, main text). (b) Excitations of the Ψ_3 ground state, for exchange parameters on the boundary between the Ψ_3 and FM phases, i.e. $J_1 = -0.029\text{meV}$, $J_2 = -0.22\text{meV}$, $J_3 = -0.29\text{meV}$ with $J_4 = 0$. The Ψ_3 phase, on the phase boundary also possesses a quasi-flat band along (h, h, h) , which in this case is gapless at the Γ point of the Brillouin zone. This leads us to suggest that the low energy rod like features observed in the paramagnetic phase of $\text{Yb}_2\text{Ti}_2\text{O}_7$ arise from its proximity in parameter space to the Ψ_3 phase and the low energy modes which are present on the phase boundary.

Using this basis, the fluctuations on site i of tetrahedron k can be parameterized as

$$\mathbf{S}_{ik} = \begin{pmatrix} \sqrt{S}\delta u_{ik} \\ \sqrt{S}\delta v_{ik} \\ \sqrt{S^2 - S\delta u_{ik}^2 - S\delta v_{ik}^2} \end{pmatrix} \approx \begin{pmatrix} \sqrt{S}\delta u_{ik} \\ \sqrt{S}\delta v_{ik} \\ S - \frac{1}{2}\delta u_{ik}^2 - \frac{1}{2}\delta v_{ik}^2 \end{pmatrix}. \quad (\text{F2})$$

Substituting Eq. (F2) into \mathcal{H}_{ex} [Eq. (A2)] we obtain

$$\mathcal{H}_{\text{ex}} = \sum_{\text{tet}} \sum_{k, i < j} \mathbf{S}_{ik} \cdot \mathbf{J}_{ij} \cdot \mathbf{S}_{jk} = \mathcal{E}_0 + \mathcal{H}_{\text{ex}}^{\text{CSW}} + \dots \quad (\text{F3})$$

where

$$\mathcal{E}_0 = \frac{NS^2}{4} \sum_{i,j=0}^3 \mathbf{w}_i \cdot \mathbf{J}_{ij} \cdot \mathbf{w}_j \quad (\text{F4})$$

is the classical ground-state energy of the chosen

4-sublattice state, and

$$\mathcal{H}_{\text{ex}}^{\text{CSW}} = \frac{S}{2} \sum_k \sum_{i,j=0}^3 \left[-\frac{1}{2}(\delta u_{ik}^2 + \delta u_{jk}^2 + \delta v_{ik}^2 + \delta v_{jk}^2)(\mathbf{w}_i \cdot \mathbf{J}_{ij} \cdot \mathbf{w}_j) + \delta u_{ik}\delta u_{jk}(\mathbf{u}_i \cdot \mathbf{J}_{ij} \cdot \mathbf{u}_j) + \delta v_{ik}\delta v_{jk}(\mathbf{v}_i \cdot \mathbf{J}_{ij} \cdot \mathbf{v}_j) + \delta u_{ik}\delta v_{jk}(\mathbf{u}_i \cdot \mathbf{J}_{ij} \cdot \mathbf{v}_j) + \delta v_{ik}\delta u_{jk}(\mathbf{v}_i \cdot \mathbf{J}_{ij} \cdot \mathbf{u}_j) \right] \quad (\text{F5})$$

describes the leading effect of (classical) fluctuations about this state. Performing Fourier transformation, we find

$$\mathcal{H}_{\text{ex}}^{\text{CSW}} = \frac{NS^2}{4} \sum_{i,j=0}^3 \mathbf{w}_i \cdot \mathbf{J}_{ij} \cdot \mathbf{w}_j + \frac{1}{2} \sum_{\mathbf{q}} \tilde{u}(-\mathbf{q})^T \cdot \mathbf{M}(\mathbf{q}) \cdot \tilde{u}(\mathbf{q}) \quad (\text{F6})$$

Here $\tilde{u}(\mathbf{q})$ is the vector

$$\tilde{u}(\mathbf{q}) = \begin{pmatrix} \delta\tilde{u}_0(\mathbf{q}), \delta u_1(\mathbf{q}), \delta u_2(\mathbf{q}), \delta u_3(\mathbf{q}), \\ \delta v_0(\mathbf{q}), \delta v_1(\mathbf{q}), \delta v_2(\mathbf{q}), \delta v_3(\mathbf{q}) \end{pmatrix}^T, \quad (\text{F7})$$

and $\mathbf{M}(\mathbf{q})$ the 8×8 matrix

$$\mathbf{M}(\mathbf{q}) = 2S \begin{pmatrix} \mathbf{M}^{11}(\mathbf{q}) & \mathbf{M}^{12}(\mathbf{q}) \\ \mathbf{M}^{21}(\mathbf{q}) & \mathbf{M}^{22}(\mathbf{q}) \end{pmatrix} \quad (\text{F8})$$

built 4×4 blocks

$$\mathbf{M}_{ij}^{11}(\mathbf{q}) = \cos(\mathbf{q} \cdot \mathbf{r}_{ij}) \left(\mathbf{u}_i \cdot \mathbf{J}_{ij} \cdot \mathbf{u}_j - \delta_{ij} \sum_l (\mathbf{w}_l \cdot \mathbf{J}_{lj} \cdot \mathbf{w}_j) \right) \quad (\text{F9})$$

$$\mathbf{M}_{ij}^{12}(\mathbf{q}) = \mathbf{M}_{ji}^{21}(\mathbf{q}) = \cos(\mathbf{q} \cdot \mathbf{r}_{ij}) \left(\mathbf{v}_i \cdot \mathbf{J}_{ij} \cdot \mathbf{u}_j \right) \quad (\text{F10})$$

$$\mathbf{M}_{ij}^{22}(\mathbf{q}) = \cos(\mathbf{q} \cdot \mathbf{r}_{ij}) \left(\mathbf{v}_i \cdot \mathbf{J}_{ij} \cdot \mathbf{v}_j - \delta_{ij} \sum_l (\mathbf{w}_l \cdot \mathbf{J}_{lj} \cdot \mathbf{w}_j) \right) \quad (\text{F11})$$

where $i, j \in \{0, 1, 2, 3\}$ and $\mathbf{r}_{ij} = \mathbf{r}_j - \mathbf{r}_i$ [cf. Eq. (A1)].

The matrix $\mathbf{M}(\mathbf{q})$ [Eq. (F8)] can be diagonalized by a suitable orthogonal transformation, $\mathbf{U} = (\mathbf{U}^T)^{-1}$ to give

$$\mathcal{H}_{\text{ex}}^{\text{CSW}} = \frac{1}{2} \sum_{\mathbf{q}} \sum_{\nu=1}^8 \kappa_{\nu\mathbf{q}} v_{\nu\mathbf{q}} v_{\nu-\mathbf{q}} \quad (\text{F12})$$

where the eight normal modes of the system are given by $v(\mathbf{q}) = \mathbf{U} \cdot \tilde{u}(\mathbf{q})$ with associated eigenvalues $\kappa_{\nu}(\mathbf{q})$. Since $\mathcal{H}_{\text{ex}}^{\text{CSW}}$ [Eq. (F12)] is quadratic in $v_{\nu\mathbf{q}}$, the associated partition function can be calculated exactly

$$\begin{aligned} \mathcal{Z}_{\text{ex}}^{\text{CSW}} &= \frac{1}{\sqrt{2\pi}} \int \prod_{\nu=1}^8 \prod_{\mathbf{q}} dv_{\nu\mathbf{q}} \\ &\exp \left(-\frac{1}{2} \frac{\sum_{\nu=1}^8 \sum_{\mathbf{q}} \kappa_{\nu\mathbf{q}} v_{\nu\mathbf{q}} v_{i-\mathbf{q}}}{T} \right) \\ &= \prod_{\nu=1}^8 \prod_{\mathbf{q}} \left(\sqrt{\frac{T}{\kappa_{\nu\mathbf{q}}}} \right). \end{aligned} \quad (\text{F13})$$

It follows that, for $T \rightarrow 0$, the free energy of the system is given by

$$\mathcal{F}_{\text{ex}}^{\text{low-T}} = \mathcal{E}_0 - \frac{T}{2} \sum_{\mathbf{q}} \ln \kappa_{\nu\mathbf{q}} + N(T \ln T + T) + \mathcal{O}(T^2) \quad (\text{F14})$$

Within this classical, low-T expansion, the eigenvalues $\kappa_{\nu}(\mathbf{q})$ correspond to independent, low energy modes,

which determine the physical properties of the states, and have the interpretation of a classical spin-wave spectrum. This is illustrated for the non-collinear FM, with parameters appropriate for $\text{Yb}_2\text{Ti}_2\text{O}_7$, in Fig. 15. However the classical spectrum $\kappa_{\nu}(\mathbf{q})$ should *not* be confused with the semi-classical spin-wave dispersion $\omega_{\nu}(\mathbf{q})$ found in linear spin-wave theory, where quantum effects are included.

Appendix G: Ground-state selection within the one-dimensional manifold of states with E symmetry

Knowledge of the free energy $\mathcal{F}_{\text{ex}}^{\text{low-T}}$ [Eq. (F14)] makes it possible to determine which of possible E symmetry ground states is selected by thermal fluctuations in the limit $T \rightarrow 0$.

Expanding the free energy in components of \mathbf{m}_{E} [cf. Eq. (D8)], we find

$$\begin{aligned} \mathcal{F}_{\text{E}} &= \mathcal{F}_0 + \frac{1}{2} a m_{\text{E}}^2 + \frac{1}{4} b m_{\text{E}}^4 + \frac{1}{6} c m_{\text{E}}^6 \\ &+ \frac{1}{6} d m_{\text{E}}^6 \cos(6\theta_{\text{E}}) + \mathcal{O}(m_{\text{E}}^8) \end{aligned} \quad (\text{G1})$$

where \mathcal{F}_0 is an unimportant constant. It follows that (1) a suitable (secondary) order parameter for symmetry breaking within this manifold is $c_{\text{E}} = \cos 6\theta_{\text{E}}$ [cf. Eq. (D10)], and that (2) the two states spanning \mathbf{m}_{E} , Ψ_2 and Ψ_3 , are distinguished only at sixth-order in m_{E} [30]. These facts have important consequences for the finite temperature phase transition into the paramagnet, as discussed below.

For $T \rightarrow 0$, we can parameterise \mathcal{F}_{E} [Eq. (G1)] from $\mathcal{F}_{\text{ex}}^{\text{low-T}}$ [Eq. (F14)]. Since $\mathcal{H}'_{\text{ex}}^{[\text{Td}]}$ [Eq. (C2)] is quadratic in \mathbf{m}_{E} , all other terms in the free energy must be of purely entropic origin. Moreover, from the form of \mathcal{F}_{E} , we anticipate that the entropy associated with the E-symmetry states will vary as

$$\mathcal{S}_{\text{E}}(\theta_{\text{E}}) = N \sum_{n=0,1,2,\dots} s_n \cos(6n\theta_{\text{E}}) \quad (\text{G2})$$

The sign of the coefficients s_n then determines the ground state selected by fluctuations. This expectation is confirmed by explicit calculation of

$$\frac{\mathcal{S}_{\text{E}}(\theta_{\text{E}})}{N} = \ln T + 1 - \frac{1}{2N} \sum_{\mathbf{q}} \ln(\det(\mathbf{M}(\mathbf{q}))) \quad (\text{G3})$$

[cf. Ref. 54], where $\mathbf{M}(\mathbf{q})$ is the 8×8 matrix defined in Eq. (F8). These results are illustrated in Fig. 16. Equivalent calculations, carried out numerically for all parameters associated with E-symmetry ground states, lead to the phase boundary between Ψ_2 and Ψ_3 shown in Fig. 1 of the main text. For parameters appropriate to $\text{Er}_2\text{Ti}_2\text{O}_7$ [28], we find that fluctuations select a Ψ_2 ground state, in keeping with earlier published work on quantum fluctuations^{25,28,29}

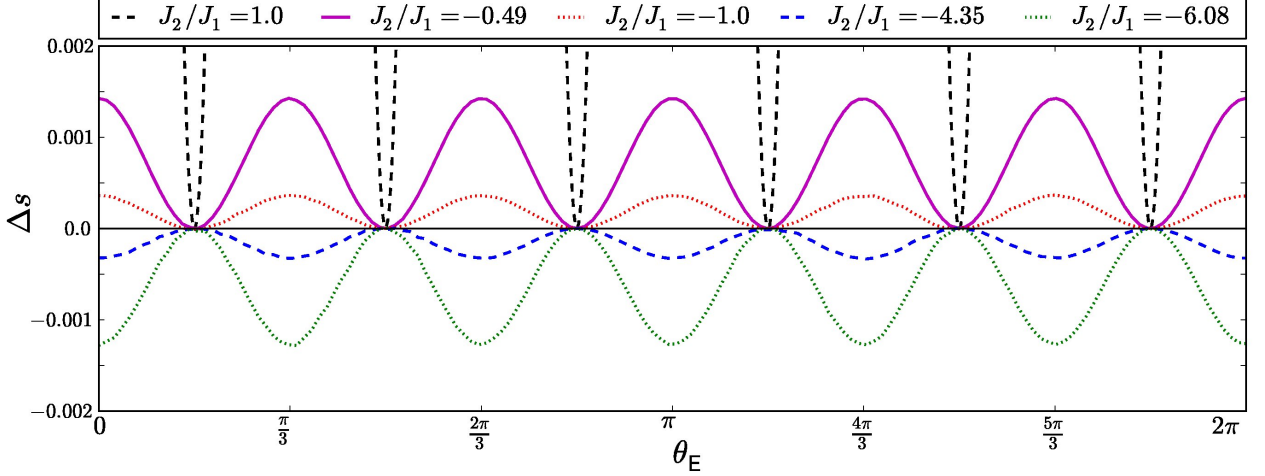


FIG. 16: Variation of entropy per spin within the one-dimensional manifold of states with symmetry E. Entropy $\mathcal{S}(\theta_E)$ has been estimated using the low-temperature expansion [Eq. (G3)], for a range of values of J_2 , with the entropy of the Ψ_3 state subtracted as a reference, i.e. $\Delta s_{\theta_E} = [\mathcal{S}(\theta_E) - \mathcal{S}(\pi/6)]/N$. The parameters $J_1 = 0.115\text{meV}$ and $J_3 = -0.099\text{meV}$ were fixed at values appropriate to $\text{Er}_2\text{Ti}_2\text{O}_7$ [28], setting $J_4 \equiv 0$. In all cases, Δs_{θ_E} repeats with period $2\pi/6$. For a choice of J_2 appropriate to $\text{Er}_2\text{Ti}_2\text{O}_7$ [$J_2/J_1 = -0.49$ — solid purple line], entropy takes on its maximum value for $\theta_E = \frac{n\pi}{3}$, with $n = 0, 1, 2, 3, 4, 5$, corresponding to the six Ψ_2 ground states. The extreme variation in entropy at the boundary of the Palmer-Chalker phase [$J_1 = J_2$ — dashed black line], reflects the presence of an $\mathcal{O}(L^2)$ set of zero modes in the spectrum of the Ψ_2 ground state. None the less, the entropy difference between Ψ_2 and Ψ_3 , $\Delta s_{\pi/3} \approx 0.18$ remains finite. For sufficiently negative J_2 (dashed blue line, dotted yellow line) $\Delta s_{\pi/3} < 0$, and fluctuations select the Ψ_3 state. All results have been calculated from Eq. (G3), with the sum evaluated numerically by a Monte Carlo method. Statistical errors are smaller than the point size.

We can now learn more about how ground state selection works by realising that, for some choices of parameters, the operation connecting different E-symmetry ground states becomes an *exact* symmetry of the Hamiltonian. This is most easily seen by writing \mathcal{H}_{ex} [Eq. (A2)] in a coordinate frame tied to the local [111] axes. Following the notation of [26],

$$\begin{aligned} \mathcal{H}'_{\text{ex}} = \sum_{\langle ij \rangle} & \left\{ J_{zz} S_i^z S_j^z - J_{\pm} (S_i^+ S_j^- + S_i^- S_j^+) \right. \\ & + J_{\pm\pm} [\gamma_{ij} S_i^+ S_j^+ + \gamma_{ij}^* S_i^- S_j^-] \\ & \left. + J_{z\pm} [S_i^z (\zeta_{ij} S_j^+ + \zeta_{ij}^* S_j^-) + i \leftrightarrow j] \right\} \quad (\text{G4}) \end{aligned}$$

where S_i^α are the transformed spins,

$$J_{zz} = -\frac{1}{3}(2J_1 - J_2 + 2(J_3 + 2J_4)) \quad (\text{G5})$$

$$J_{\pm} = \frac{1}{6}(2J_1 - J_2 - J_3 - 2J_4) \quad (\text{G6})$$

$$J_{\pm\pm} = \frac{1}{6}(J_1 + J_2 - 2J_3 + 2J_4) \quad (\text{G7})$$

$$J_{z\pm} = \frac{1}{3\sqrt{2}}(J_1 + J_2 + J_3 - J_4) \quad (\text{G8})$$

and the matrices

$$\zeta = \begin{pmatrix} 0 & -1 & e^{i\frac{\pi}{3}} & e^{-i\frac{\pi}{3}} \\ -1 & 0 & e^{-i\frac{\pi}{3}} & e^{i\frac{\pi}{3}} \\ e^{i\frac{\pi}{3}} & e^{-i\frac{\pi}{3}} & 0 & -1 \\ e^{-i\frac{\pi}{3}} & e^{i\frac{\pi}{3}} & -1 & 0 \end{pmatrix} \quad \gamma = -\zeta^* \quad (\text{G9})$$

encode the rotations in co-ordinate frame between different sublattices.

For the simple choice

$$(J_{zz}, J_{\pm}, J_{\pm\pm}, J_{z\pm}) = (0, J, 0, 0) \quad J > 0$$

the ground state belongs to E and \mathcal{H}'_{ex} [Eq. (G4)] reduces to an XY ferromagnet. In this case the entire one-dimensional manifold of E-symmetry states are connected by an explicit symmetry of the Hamiltonian (rotation around the local (111) axes). It follows that order-by-disorder is ineffective, and the ground state retains its $U(1)$ symmetry — for a related discussion, see [43].

To gain insight into the phase diagram for $J_3 < 0$, $J_4 \equiv 0$ [cf. Fig. 1, main text], we expand about a point in parameter space

$$\begin{aligned} (J_{zz}, J_{\pm}, J_{\pm\pm}, J_{z\pm}) &= (-2J, J, 0, 0) \quad J > 0 \\ \implies (J_1, J_2, J_3, J_4) &= (2J, -2J, 0, 0) \end{aligned}$$

where \mathcal{H}'_{ex} [Eq. (G4)] reduces to a Heisenberg ferromagnet. At this point the ground state manifold is formed from linear combinations of E and A_2 symmetry states and all the entire ground state manifold is connected by an exact symmetry of the Hamiltonian, so one again there is no order by disorder. For $J_3 < 0$ states with a finite value of m_{A_2} are removed from the ground state manifold and fluctuations select a ground state from amongst the E states. It follows that, for $J_3 \rightarrow 0^-$, $J_4 \equiv 0$, the phase boundary between the Ψ_2 and Ψ_3 states should tend to the line $J_2/|J_3| = -J_1/|J_3|$ [cf. Fig. 1, main text].

To see which phase is preferred for finite J_3 , we expand the difference in entropy $\mathcal{S}_E(\theta_E)$ between the Ψ_2 and Ψ_3 ground states

$$\Delta s_{\pi/3} = \frac{\mathcal{S}_E(\pi/3) - \mathcal{S}_E(\pi/6)}{N} \quad (\text{G10})$$

in powers of $J_{\pm\pm}$ and $J_{z\pm}$. We do this by writing the matrix $\mathbf{M}(\mathbf{q})$ [Eq. F8] as

$$\mathbf{M}(\mathbf{q}) = \mathbf{M}_0(\mathbf{q}) + \epsilon \mathbf{X}(\mathbf{q}) \quad (\text{G11})$$

where $\mathbf{M}_0(\mathbf{q})$ is the matrix associated with the high-symmetry point, and $\mathbf{X}(\mathbf{q})$ that associated with the perturbation, and noting that

$$\begin{aligned} \ln(\det(\mathbf{M}_0 + \epsilon \mathbf{X})) &= \ln(\det(\mathbf{M}_0)) \\ &+ \sum_{n=1}^{\infty} (-1)^{(n+1)} \frac{\epsilon^n}{n} \text{Tr} \left[(\mathbf{X} \cdot \mathbf{M}_0^{-1})^n \right]. \end{aligned} \quad (\text{G12})$$

We then expand in powers of $J_{\pm\pm}$ and $J_{z\pm}$.

We find that the leading correction to ΔS is

$$\Delta s_{\pi/3} \approx a \left(\frac{J_{\pm\pm}}{J_{\pm}} \right)^3 \quad (\text{G13})$$

where $a = 0.0045$. It follows that, for sufficiently small J_3 , the phase boundary between Ψ_2 and Ψ_3 should tend to the line $J_{\pm\pm} = 0$, with the Ψ_2 phase favoured for $J_{\pm\pm} > 0$ and Ψ_3 favoured for $J_{\pm\pm} < 0$. Numerical evaluation of Eq. G3, in the limit $J_3 \rightarrow 0$, yields results in agreement with these arguments [cf. Fig. 1, main text].

On the line $J_{\pm\pm} = 0$ itself, we find that the leading correction to the difference in entropy is

$$\Delta s_{\pi/3} \approx b \left(\frac{J_{z\pm}}{J_{\pm}} \right)^6 \quad (\text{G14})$$

with $b = -5.3 \times 10^{-5}$. Hence the Ψ_3 state is weakly preferred, and the phase boundary will bend towards positive $J_2/|J_3|$, as observed in Fig. 1 of the main text. Since $J_{z\pm}$ is a term which drives out of plane fluctuations, a negative sign for b is consistent with the argument that Ψ_3 is better connected to the ferromagnetic phase, and hence has a softer spectrum for out-of-plane fluctuations.

In the limit $|J_3| \gtrsim (|J_1|, |J_2|)$, numerical evaluation of Eq. G3 yields the more complex, reentrant behaviour, as seen in Fig. 1 of the main text. This behaviour occurs over a very narrow region of parameter space, and is discussed in detail (for the case of quantum, as opposed to thermal order by disorder) in [43].

Appendix H: Semiclassical spin wave theory

The effect of quantum fluctuations on ordered states can be estimated with a conventional large- S expansion. The sublattice dependent basis $\{\mathbf{u}_i, \mathbf{v}_i, \mathbf{w}_i\}$, previously introduced for classical spins [Eq. (F2)], again provides

a convenient starting point. Working to leading order in Holstein-Primakoff bosons $[a_i, a_j^\dagger] = \delta_{ij}$, we write

$$S_i^w = S - a_i^\dagger a_i \quad (\text{H1})$$

$$S_i^+ = S_i^u + iS_i^v = (2S - a_i^\dagger a_i)^{1/2} a_i \approx \sqrt{2S} a_i \quad (\text{H2})$$

$$S_i^- = S_i^u - iS_i^v = a_i^\dagger (2S - a_i^\dagger a_i)^{1/2} \approx \sqrt{2S} a_i^\dagger \quad (\text{H3})$$

Substituting these expressions in \mathcal{H}_{ex} [Eq. (A2)] and Fourier transforming them, we obtain

$$\mathcal{H}_{\text{ex}} = \mathcal{E}_0 + \mathcal{H}_{\text{ex}}^{\text{LSW}} + \dots \quad (\text{H4})$$

where \mathcal{E}_0 is the classical ground state energy defined in Eq. (F4), and

$$\mathcal{H}_{\text{ex}}^{\text{LSW}} = \frac{1}{2} \sum_{\mathbf{q}} \tilde{A}_i^\dagger(\mathbf{q}) \cdot \mathbf{X}(\mathbf{q}) \cdot \tilde{A}(\mathbf{q}) \quad (\text{H5})$$

describes quantum fluctuations at the level of linear spin wave theory. Here $\tilde{A}^\dagger(\mathbf{q}), \tilde{A}(\mathbf{q})$ are eight-component vectors of operators

$$\begin{aligned} \tilde{A}^\dagger(\mathbf{q}) &= (a_0^\dagger(\mathbf{q}), a_1^\dagger(\mathbf{q}), a_2^\dagger(\mathbf{q}), a_3^\dagger(\mathbf{q}), \\ &a_0(-\mathbf{q}), a_1(-\mathbf{q}), a_2(-\mathbf{q}), a_3(-\mathbf{q})) \end{aligned} \quad (\text{H6})$$

and $\mathbf{X}(\mathbf{q})$ is an 8×8 matrix written in block form as

$$\mathbf{X}(\mathbf{q}) = 2S \begin{pmatrix} \mathbf{X}^{11}(\mathbf{q}) & \mathbf{X}^{12}(\mathbf{q}) \\ \mathbf{X}^{21}(\mathbf{q}) & \mathbf{X}^{22}(\mathbf{q}) \end{pmatrix} \quad (\text{H7})$$

$$\begin{aligned} \mathbf{X}_{ij}^{11}(\mathbf{q}) &= \cos(\mathbf{q} \cdot \mathbf{r}_{ij}) \\ &\left(\mathbf{c}_i \cdot \mathbf{J}^{ij} \cdot \mathbf{c}_j^* - \delta_{ij} \sum_l \mathbf{w}_l \cdot \mathbf{J}^{lj} \cdot \mathbf{w}_j \right) \end{aligned} \quad (\text{H8})$$

$$\mathbf{X}_{ij}^{12}(\mathbf{q}) = \mathbf{X}_{ji}^{21*} = \cos(\mathbf{q} \cdot \mathbf{r}_{ij}) \left(\mathbf{c}_i \cdot \mathbf{J}^{ij} \cdot \mathbf{c}_j \right) \quad (\text{H9})$$

$$\begin{aligned} \mathbf{X}_{ij}^{22}(\mathbf{q}) &= \cos(\mathbf{q} \cdot \mathbf{r}_{ij}) \\ &\left(\mathbf{c}_i^* \cdot \mathbf{J}^{ij} \cdot \mathbf{c}_j - \delta_{ij} \sum_l \mathbf{w}_l \cdot \mathbf{J}^{lj} \cdot \mathbf{w}_j \right) \end{aligned} \quad (\text{H10})$$

where

$$\mathbf{c}_i = \frac{1}{\sqrt{2}} (\mathbf{u}_i + i\mathbf{v}_i). \quad (\text{H11})$$

The spin-wave Hamiltonian $\mathcal{H}_{\text{ex}}^{\text{LSW}}$ [Eq. (H5)] can be diagonalized by a suitable Bogoliubov transformation. We accomplish this following the method outlined in Ref. 55 by introducing new Bose operators $[b_i, b_j^\dagger] = \delta_{ij}$, such that

$$\begin{aligned} B^\dagger(\mathbf{q}) &= (b_0^\dagger(\mathbf{q}), b_1^\dagger(\mathbf{q}), b_2^\dagger(\mathbf{q}), b_3^\dagger(\mathbf{q}), \\ &b_0(-\mathbf{q}), b_1(-\mathbf{q}), b_2(-\mathbf{q}), b_3(-\mathbf{q})) \\ &= A^\dagger(\mathbf{q}) \cdot \mathbf{U}^\dagger(\mathbf{q}) \end{aligned} \quad (\text{H12})$$

The condition that these operators are Bosonic

$$[B_i(\mathbf{q}), B_j^\dagger(\mathbf{q}')] = \sigma_{ij} \delta_{\mathbf{q}\mathbf{q}'} \quad (\text{H13})$$

where

$$\hat{\sigma} = \begin{pmatrix} \mathbf{1} & \mathbf{0} \\ \mathbf{0} & -\mathbf{1} \end{pmatrix}. \quad (\text{H14})$$

is an 8×8 matrix (written in block form), and

$$\left[B_i^\dagger(\mathbf{q}), B_j^\dagger(\mathbf{q}') \right] = \left[B_i(\mathbf{q}), B_j(\mathbf{q}') \right] = 0 \quad (\text{H15})$$

leads to a pseudo-unitary condition on $\mathbf{U}(\mathbf{q})$

$$\mathbf{U}^{-1}(\mathbf{q}) = \hat{\sigma} \cdot \mathbf{U}^\dagger(\mathbf{q}) \cdot \hat{\sigma}. \quad (\text{H16})$$

Substituting in Eq. H5, we obtain

$$\begin{aligned} \mathcal{H}_{\text{ex}}^{\text{LSW}} &= \frac{1}{2} \sum_{\mathbf{q}} B^\dagger(\mathbf{q}) \cdot \mathbf{U}^{-1\dagger}(\mathbf{q}) \cdot \vec{X}(\mathbf{q}) \cdot \mathbf{U}^{-1}(\mathbf{q}) \cdot B(\mathbf{q}) \\ &= \frac{1}{2} \sum_{\mathbf{q}} B^\dagger(\mathbf{q}) \cdot \sigma \cdot \mathbf{U}(\mathbf{q}) \cdot \sigma \cdot \vec{X}(\mathbf{q}) \cdot \mathbf{U}^{-1}(\mathbf{q}) \cdot B(\mathbf{q}). \end{aligned} \quad (\text{H17})$$

The object $\mathbf{U}(\mathbf{q}) \cdot \sigma \cdot \vec{X}(\mathbf{q}) \cdot \mathbf{U}^{-1}(\mathbf{q})$ is a similarity transformation on the matrix $\sigma \cdot \vec{X}(\mathbf{q})$, and for correctly chosen $\mathbf{U}(\mathbf{q})$, will be a diagonal matrix containing the eigenvalues of $\sigma \cdot \vec{X}(\mathbf{q})$. We then arrive at

$$\mathcal{H}_{\text{ex}}^{\text{LSW}} = \frac{1}{2} \sum_{\mathbf{q}} B^\dagger(\mathbf{q}) \cdot \sigma \cdot \begin{pmatrix} \omega_\nu(\mathbf{k}) & 0 \\ 0 & -\omega_\nu(\mathbf{k}) \end{pmatrix} \cdot B(\mathbf{q}). \quad (\text{H18})$$

Collecting all terms and reordering operators, we have

$$\begin{aligned} \mathcal{H}_{\text{ex}} &= \mathcal{E}_0 \left(1 + \frac{1}{S} \right) \\ &+ \sum_{\mathbf{q}} \sum_{\nu=0}^3 \omega_\nu(\mathbf{q}) \left(b_\nu^\dagger(\mathbf{q}) b_\nu(\mathbf{q}) + \frac{1}{2} \right) + \dots \end{aligned} \quad (\text{H19})$$

The dispersion $\omega_\nu(\mathbf{q})$ of the four branches of spin waves can be found by numerical diagonalization of $\sigma \cdot \vec{X}(\mathbf{q})$.

The effect of quantum fluctuations on classical order may be estimated by calculating the correction to the ordered moment on sublattice i

$$\begin{aligned} \langle S_w^i \rangle &= S - \langle a_i^\dagger a_i \rangle \\ &= S - \frac{4}{N} \sum_{\mathbf{q}} \sum_{m=4}^7 |\mathbf{U}_{im}(\mathbf{q})|^2 \end{aligned} \quad (\text{H20})$$

where $\sum_{m=4}^7$ implies a sum over the off-diagonal 4×4 block of $\mathbf{U}(\mathbf{q})$. In all of the 4-sublattice phases described in this text, $\langle S_w^i \rangle$ is the same for all sublattices $i = 0, 1, 2, 3$.

The results of this analysis are shown in Fig. 6 of the main text, where we show that divergences in the ordered moment correction approaching the high degeneracy limits of the model lead to regions where the conventional magnetic order is completely eliminated.

Appendix I: Classical Monte Carlo simulation

The Monte Carlo simulations in this paper are based on the Metropolis algorithm with parallel tempering^{56,57} and over-relaxation⁵⁸. The spins are modelled as classical vectors of length $|S_i| = 1/2$ and locally updated using the standard Marsaglia method⁵⁹. We consider cubic clusters of linear dimension L , based on the 16-site cubic unit cell of the pyrochlore lattice, and containing $N = 16L^3$ sites. A Monte Carlo step (MCs) is defined as N attempts to locally update a randomly chosen spin, and t_{max} (measured in MCs) is the total Monte Carlo time over which data are collected.

Equilibration is performed for each temperature in two successive steps. First the system is slowly cooled down from high temperature (random initial spin configuration) to the temperature of measurement T during $t_{max}/10$ MCs. Then, the system is equilibrated at temperature T during additional $t_{max}/10$ MCs. After equilibration, Monte Carlo time is set to zero and measurements start and go on for $t_{max} \sim 10^5 - 10^7$ MCs.

All thermodynamical observables have been averaged over Monte Carlo time every 10 MCs, except for calculations of the equal-time structure factor $S(\mathbf{q})$, where data points were taken every 100 MCs for efficiency. The parallel tempering method implies simultaneously simulating a large number of replicas of the system in parallel, with each replica held at a different temperature. The program then regularly attempts to swap the spin configurations of replicas with neighbouring temperatures, in such a way as to maintain detailed balance^{56,57}. Simulating ~ 100 replicas, with swaps attempted every 100 MCs appears to offer a good compromise between efficiency and decorrelation for $L=6$.

In the case of the over-relaxation method, after each Monte Carlo step, two further sweeps are made of the entire lattice. Each spin feels an effective field due to the interaction with its six neighbours; any rotation around this axis conserves the energy and is thus an acceptable move respecting detailed balance. To avoid rotating successive neighbouring spins, we first update all spins of sublattice 0, then sublattice 1, 2 and finally 3. The first iteration of all N spins is deterministic, *i.e.* we rotate them by the maximum allowed angle; while for the second iteration, a random angle of rotation is chosen for each spin. The generation of so many random numbers is of course time consuming but is recommended for better equilibration⁶⁰. We note that convergence of the specific heat $c_h \rightarrow 1$ for $T \rightarrow 0$ is a good indication of the equilibration at low temperatures.

Appendix J: Finite temperature phase diagram

1. Details of simulations

In Fig. 3 of the main text we show a finite temperature phase diagram spanning all four of the ordered phases dis-

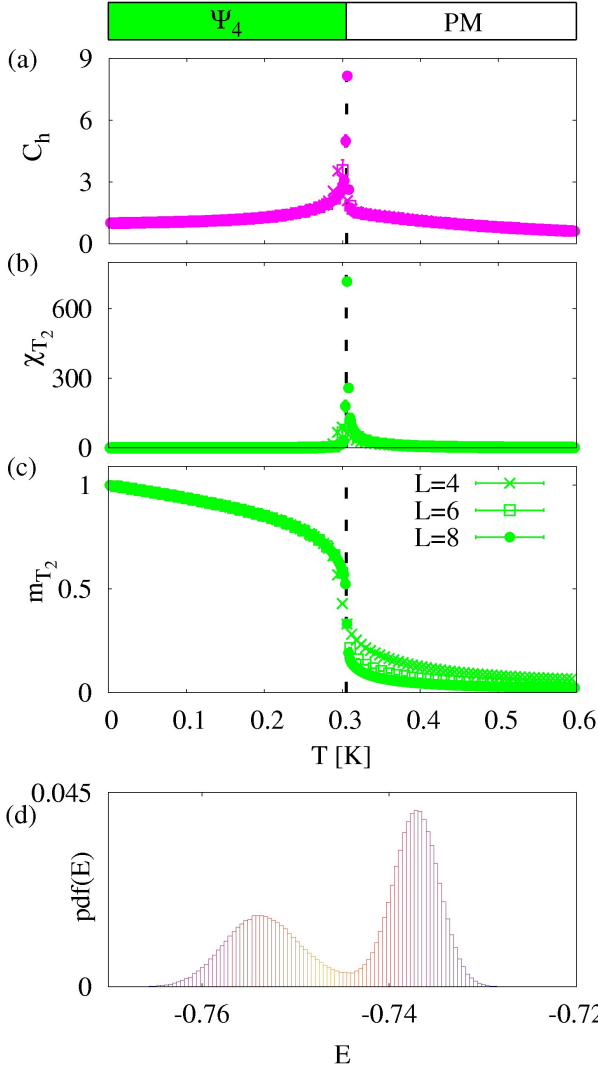


FIG. 17: Finite-temperature phase transition from the paramagnet into the Palmer-Chalker phase $[\Psi_4]$, as determined by classical Monte Carlo simulation of \mathcal{H}_{ex} [Eq. (A2)], for parameters $J_1 = 0$ meV, $J_2 = 0.3$ meV, $J_3 = -0.1$ meV, $J_4 = 0$ meV. a) Temperature dependence of the specific heat $c_h(T)$. b) Temperature dependence of the order-parameter susceptibility, $\chi_{T_2}(T)$. c) Temperature dependence of the order parameter, $|\mathbf{m}_{T_2}(T)|$. d) Probability distribution of the energy E evaluated at the transition temperature $T_c = 306.5$ mK for a cluster of size $L = 12$. The black dashed line in (a)-(c) indicates a first-order phase transition at $T_{T_2} = 305 \pm 5$ mK. Simulations were performed for clusters of $N = 16L^3$ spins, with $L = 4, 6, 8, 12$.

cussed in the article. This phase diagram was determined from simulations for 64 different parameter sets, equally spaced on the circle defined by $\sqrt{J_1^2 + J_2^2} = 3|J_3|$ with $J_3 = -0.1$ meV and $J_4 = 0$ [cf. white circle in Fig. 1 of main text]. Transition temperatures for each phase were extracted from the relevant order-parameter susceptibilities. This is described in turn for each of the four ordered phases, below.

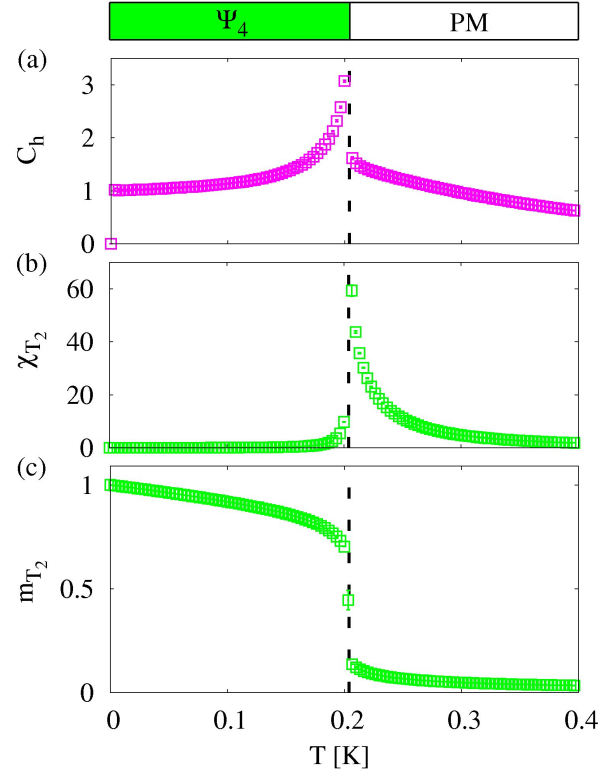


FIG. 18: Finite-temperature phase transition from the paramagnet into the Palmer-Chalker phase $[\Psi_4]$, as determined by classical Monte Carlo simulation of \mathcal{H}_{ex} [Eq. (A2)], for parameters appropriate to $\text{Er}_2\text{Sn}_2\text{O}_7$ [18], i.e. $J_1 = 0.07$ meV, $J_2 = 0.08$ meV, $J_3 = -0.11$ meV, $J_4 = 0.04$ meV. a) Temperature dependence of the specific heat $c_h(T)$. b) Temperature dependence of the order-parameter susceptibility, $\chi_{T_2}(T)$. c) Temperature dependence of the order parameter, $|\mathbf{m}_{T_2}(T)|$. The black dashed line in (a)-(c) indicates a first-order phase transition at $T_{T_2} = 204 \pm 5$ mK. Simulations were performed for clusters of $N = 16L^3$ spins, with $L = 6$.

Simulations were performed for a cluster of $N = 3456$ spins ($L = 6$), and data averaged over 10 independent runs during $t_{\text{max}} = 10^6$ MCs. Parallel tempering was used, typically with 121 replicas, at temperatures equally-spaced from 0 to 1.2 K. However, close to the boundaries between phases with different symmetries, the large number of competing ground states makes simulations difficult to equilibrate. Here, additional data points with better statistics were sometimes necessary, typically with 201 temperatures on a smaller temperature window, with $t_{\text{max}} = 10^7$ MCs and $N = 8192$ (i.e. $L=8$). Under such conditions, over-relaxation was usually not necessary to determine the transition temperature.

2. Transition from the paramagnet into the Palmer-Chalker phase, $J_4 \equiv 0$

In Fig. 17 we show simulation results for the finite-temperature phase transition from the paramagnet into Palmer-Chalker phase for parameters

$$(J_1, J_2, J_3, J_4) = (0, 0.3, -0.1, 0) \text{ meV}$$

deep within the Palmer-Chalker phase. Anomalies in both the specific heat $c_h(T)$ [Fig. 17(a)] and order-parameter susceptibility $\chi_{\tau_2}(T)$ [Fig. 17(b)] at $T_{\tau_2} = 305 \pm 5$ mK, provide clear evidence of a phase transition.

For this parameter set, the transition is first order, as is evident from the discontinuity in the value of the order parameter \mathbf{m}_{τ_2} for $T = T_{\tau_2}$ [Fig. 17(c)], and double peak in the probability distribution for the energy [Fig. 17(d)].

3. Transition from the paramagnet into the Palmer-Chalker phase, for parameters appropriate to $\text{Er}_2\text{Sn}_2\text{O}_7$, $J_4 \neq 0$

In Fig. 18 we show simulation results for the finite-temperature phase transition from the paramagnet into Palmer-Chalker phase for parameters appropriate to $\text{Er}_2\text{Sn}_2\text{O}_7$

$$(J_1, J_2, J_3, J_4) = (0.07, 0.08, -0.11, 0.04) \text{ meV}$$

near to the boundary of the Palmer-Chalker phase. Anomalies in both the specific heat $c_h(T)$ [Fig. 18(a)] and order-parameter susceptibility $\chi_{\tau_2}(T)$ [Fig. 18(b)] at $T_{\tau_2} = 200 \pm 5$ mK, provide clear evidence of a phase transition. No ordering transition has ever been observed in experiment on $\text{Er}_2\text{Sn}_2\text{O}_7$, although anomalies in the magnetic susceptibility below $T = 200$ mK have been interpreted as evidence of spin freezing.

For this parameter set, the transition is first order, as is evident from the discontinuity in the value of the order parameter \mathbf{m}_{τ_2} for $T = T_{\tau_2}$ [Fig. 18(c)]. We have confirmed by repeating simulations with $J_4 \equiv 0$ that Dzyaloshinskii-Moriya interactions do not have any qualitative effect on the thermodynamics of $\text{Er}_2\text{Sn}_2\text{O}_7$. However the finite value of J_4 does have an effect on the transition temperature, which drops to $T_{\tau_2} \approx 70$ mK for $J_4 = 0$.

4. Transition from the paramagnet into the ferromagnetic phase, for parameters appropriate to $\text{Yb}_2\text{Ti}_2\text{O}_7$

In Fig. 19 we show simulation results for the finite-temperature phase transition from the paramagnet into the non-collinear ferromagnet (FM), for parameters appropriate to $\text{Yb}_2\text{Ti}_2\text{O}_7$ ²⁶, setting $J_4 = 0$

$$(J_1, J_2, J_3, J_4) = (-0.09, -0.22, -0.29, 0) \text{ meV}$$

Anomalies in both the specific heat $c_h(T)$ [Fig. 19(a)] and order-parameter susceptibility $\chi_{\tau_1}(T)$ [Fig. 19(b)] at $T_{\tau_1} = 455 \pm 5$ mK, provide clear evidence of a phase transition.

This estimate of the transition temperature compares reasonably well with experiment, where those samples which order undergo a phase transition at $T_c^{\text{Yb}_2\text{Ti}_2\text{O}_7} = 240 \pm 30$ mK^{10,44,48}. At low temperatures, the temperature-dependence of the order parameters $\mathbf{m}_{\tau_{1,A}}$ and $\mathbf{m}_{\tau_{1,B}}$ [Fig. 19(c)-(d)] converges on the values expected from a low-temperature expansion about the FM ground state (not shown).

The single peak in the probability distribution for the energy [Fig. 19(e)] suggests that, for parameters appropriate to $\text{Yb}_2\text{Ti}_2\text{O}_7$, the thermal phase transition from paramagnet to non-collinear FM in a classical model is at most very weakly first order. This contrasts with experiment, where the phase transition in those samples which order is believed to be strongly first order⁴⁸.

It is also interesting to note that classical Monte Carlo simulations for parameter sets close to the border with the Palmer-Chalker phase — where fluctuation effects are more pronounced — reveal a strongly first-order transition. We have confirmed by repeating simulations with $J_4 = 0.01$ mK (cf.²⁶) that Dzyaloshinskii-Moriya interactions have a negligible effect on the thermodynamics of $\text{Yb}_2\text{Ti}_2\text{O}_7$, changing the transition temperature to $T_{\tau_1} = 452 \pm 10$ mK

5. Transition from the paramagnet into the Ψ_2 phase, for parameters appropriate to $\text{Er}_2\text{Ti}_2\text{O}_7$

In Fig. 20 we show simulation results for the finite-temperature phase transition from the paramagnet into the Ψ_2 phase, for parameters appropriate to $\text{Er}_2\text{Ti}_2\text{O}_7$ [28], setting $J_4 = 0$

$$(J_1, J_2, J_3, J_4) = (0.11, -0.06, -0.1, 0) \text{ meV}$$

This shows a number of interesting features.

Anomalies in both the specific heat $c_h(T)$ [Fig. 20(a)] and order-parameter susceptibility $\chi_E(T)$ [Fig. 20(b)] at $T_E = 505 \pm 5$ mK offer clear evidence of a phase transition. Surprisingly, this transition occurs at a significantly *lower* temperature in simulation than experiment, where a transition is observed at $T_N^{\text{Er}_2\text{Ti}_2\text{O}_7} = 1.2 \pm 0.1$ K [10,19,30]. We have confirmed by repeating simulations with $J_4 = -0.003$ mK (cf.²⁶) that Dzyaloshinskii-Moriya interactions have a negligible effect on the thermodynamics of $\text{Er}_2\text{Ti}_2\text{O}_7$, changing the transition temperature by only a few degrees to $T_E = 506 \pm 10$ mK

Both the smooth evolution of the primary order parameter, \mathbf{m}_E [Fig. 20(c)], and the single peak in the probability distribution for the energy [Fig. 20(e)] suggests that the phase transition seen in simulation is at most weakly first-order. For the clusters simulated, we find that it is possible to obtain a fairly good collapse of data for $\chi_E(T)$ [Fig. 20(b)] using 3D XY exponents.

However there are only a discrete number of Ψ_2 ground states, and a finite value of $|\mathbf{m}_E|$ alone does not imply Ψ_2 order. Evidence for the Ψ_2 ground state comes from the secondary order parameter $c_E = \cos 6\theta_E > 0$ [Fig. 19(d)]. Here simulation results are strongly size-dependent, but suggest a slow crossover into the Ψ_2 state, occurring at a $T^* \ll T_E$, without any accompanying feature in $c_h(T)$ [Fig. 20(a)].

On the basis of the Landau theory \mathcal{F}_E [Eq. (G1)], we anticipate that *any* finite value of $m_E = |\mathbf{m}_E|$ will induce symmetry breaking in θ_E , and that both symmetries should therefore be broken at the same temperature. Depending on the sign of the relevant coupling,

$$\delta\mathcal{F}_E = \frac{1}{6} d m_E^6 \cos 6\theta_E \quad (\text{J1})$$

the system will then enter either a Ψ_2 or a Ψ_3 ground state.

However, the free-energy barrier separating the Ψ_2 and Ψ_3 ground states is very small, and this in turn sets a very large length-scale for the selection of the Ψ_2 ground state. Based on the low-temperature expansion $\mathcal{F}_{\text{ex}}^{\text{low-T}}$ [Eq. (F14)], we estimate that clusters with linear dimension $L \sim 1000$ may be needed to resolve this as a single transition.

6. Transition from the paramagnet into the Ψ_3 phase

In Fig. 21 we show simulation results for the finite-temperature phase transition from the paramagnet into the Ψ_3 phase, for parameters

$$(J_1, J_2, J_3, J_4) = (0, -0.3, -0.1, 0) \text{ meV}$$

close to the border with the non-collinear ferromagnet. Anomalies in both the specific heat $c_h(T)$ [Fig. 21(a)] and order-parameter susceptibility $\chi_E(T)$ [Fig. 21(b)] at $T_E = 395 \pm 5 \text{ mK}$ offer clear evidence of a phase transition. Both the smooth evolution of the primary order parameter, \mathbf{m}_E [Fig. 21(c)], and the single peak in the probability distribution for the energy [Fig. 21(e)] suggest that this phase transition is continuous.

Evidence for the Ψ_3 ground state comes from the finite value of the secondary order parameter $c_E = \cos 6\theta_E < 0$ [Fig. 21(d)]. This secondary order parameter shows only a slow onset, consistent with a crossover into the Ψ_3 state, and is *very* strongly size-dependent. As with the Ψ_2 state considered above, we infer that, with increasing system size, the temperature associated with this crossover scales towards $T = T_N$, and that in the thermodynamic limit, a single phase transition from takes place from the paramagnet into the Ψ_3 state.

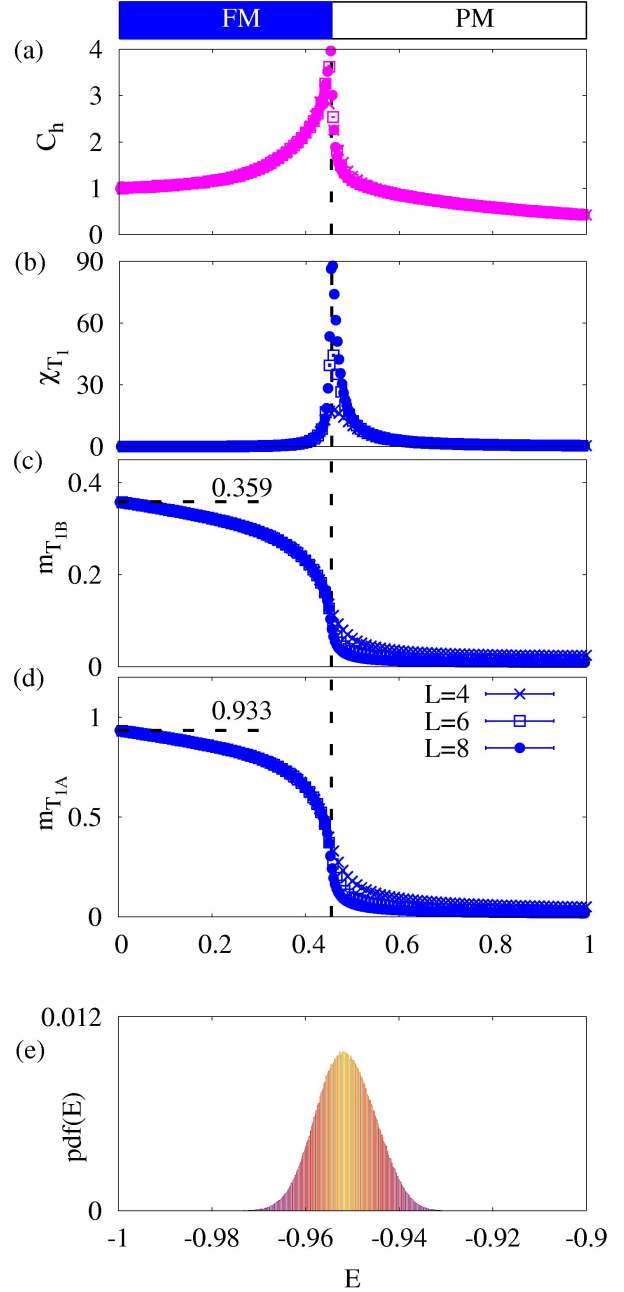


FIG. 19: Finite-temperature phase transition from the paramagnet into the non-collinear ferromagnet (FM), as determined by classical Monte Carlo simulation of \mathcal{H}_{ex} [Eq. (A2)], for parameters appropriate to $\text{Yb}_2\text{Ti}_2\text{O}_7$ ²⁶, i.e. $J_1 = -0.09 \text{ meV}$, $J_2 = -0.22 \text{ meV}$, $J_3 = -0.29 \text{ meV}$ setting $J_4 = 0 \text{ meV}$. a) Temperature dependence of the specific heat $c_h(T)$. b) Temperature dependence of the order-parameter susceptibility, $\chi_{T_1}(T)$. c) Temperature dependence of the order parameter, $|\mathbf{m}_{T_1,A}(T)|$. d) Temperature dependence of the order parameter, $|\mathbf{m}_{T_1,B}(T)|$. e) Probability distribution of the energy E evaluated at the transition for a system of size $L = 12$. The black dashed line in (a)–(d) indicates a continuous phase transition at $T_{T_1} = 455 \pm 5 \text{ mK}$. Simulations were performed for clusters of $N = 16L^3$ spins, with $L = 4, 6, 8, 12$.

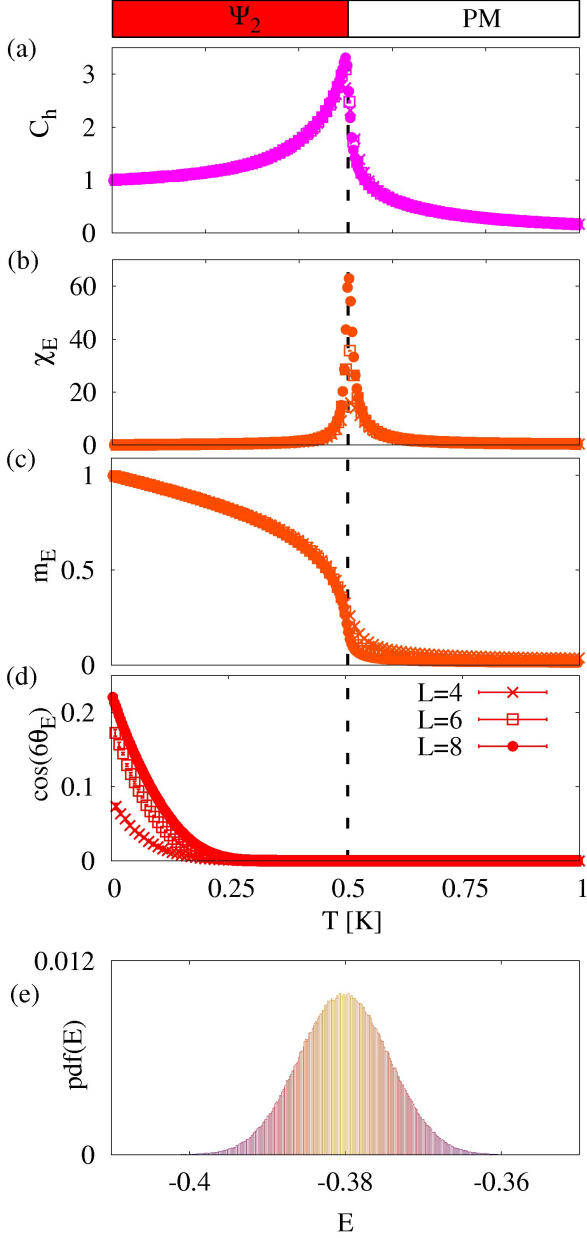


FIG. 20: Finite-temperature phase transition from the paramagnet into the non-coplanar antiferromagnet Ψ_2 , as determined by classical Monte Carlo simulation of \mathcal{H}_{ex} [Eq. (A2)], for parameters appropriate to $\text{Er}_2\text{Ti}_2\text{O}_7$ ²⁸, i.e. $J_1 = 0.11$ meV, $J_2 = -0.06$ meV, $J_3 = -0.1$ meV setting $J_4 = 0$ meV. a) Temperature dependence of the specific heat $c_h(T)$. b) Temperature dependence of the order-parameter susceptibility, $\chi_E(T)$. c) Temperature dependence of the order parameter, $|\mathbf{m}_E(T)|$. d) Temperature dependence of the order parameter, $\cos 6\theta_E$. e) Probability distribution of the energy E evaluated at the transition temperature $T_c = 502$ mK for a system of size $L = 12$. The black dashed line indicates a continuous phase transition at $T_N = 505 \pm 5$ mK. Simulations were performed for clusters of $N = 16L^3$ spins, with $L = 4, 6, 8, 12$.

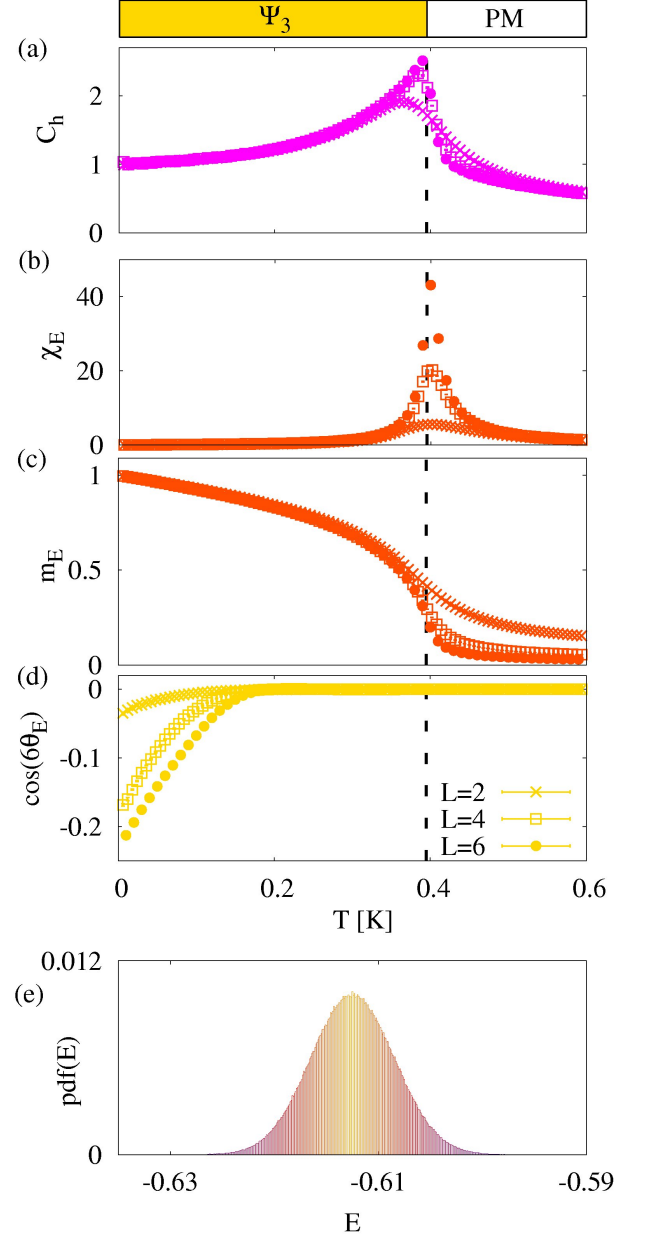


FIG. 21: Finite-temperature phase transition from the paramagnet into the coplanar antiferromagnet Ψ_3 , as determined by classical Monte Carlo simulation of \mathcal{H}_{ex} [Eq. (A2)], for parameters $J_1 = 0$ meV, $J_2 = -0.3$ meV, $J_3 = -0.1$ meV, $J_4 = 0$ meV. a) Temperature dependence of the specific heat $c_h(T)$. b) Temperature dependence of the order-parameter susceptibility, $\chi_E(T)$. c) Temperature dependence of the order parameter, $|\mathbf{m}_E(T)|$. d) Temperature dependence of the order parameter, $\cos 6\theta_E$. e) Probability distribution of the energy E evaluated at the transition temperature $T_c = 395$ mK for a system of size $L = 12$. The black dashed line indicates a continuous phase transition at $T_E = 395 \pm 5$ mK. Simulations were performed for clusters of $N = 16L^3$ spins, with $L = 2, 4, 6, 12$.

Appendix K: Equal-time structure factors $S(\mathbf{q})$

1. Definitions

The equal-time structure factor $S(\mathbf{q})$ is defined by

$$S(\mathbf{q}) = \sum_{\alpha,\beta=1}^3 \sum_{i,j=1}^4 \left(\delta_{\alpha\beta} - \frac{g_{\alpha}g_{\beta}}{q^2} \right) \langle m_{\alpha}^i(-\mathbf{q})m_{\beta}^j(\mathbf{q}) \rangle \quad (\text{K1})$$

Here the magnetic moment m_{α}^i is related to the pseudospin-1/2 via the g-tensor $S_i^{\beta}(\mathbf{R}_i)$

$$m_{\alpha}^i(\mathbf{q}) = \sqrt{\frac{4}{N}} \sum_{\beta=1}^3 g_{\alpha\beta}^i \left(\sum_{\vec{R}_i} e^{i\mathbf{q}\cdot\vec{R}_i} S_{\beta}(\vec{R}_i) \right). \quad (\text{K2})$$

In the local co-ordinate frame $\{\mathbf{x}_i^{\text{local}}, \mathbf{y}_i^{\text{local}}, \mathbf{z}_i^{\text{local}}\}$ in which the $\mathbf{z}_i^{\text{local}}$ axis is the local $\langle 111 \rangle C_3$ symmetry axis, the g-tensor is diagonal

$$\mathbf{g}^{\text{local}} = \begin{pmatrix} g_{xy} & 0 & 0 \\ 0 & g_{xy} & 0 \\ 0 & 0 & g_z \end{pmatrix} \quad (\text{K3})$$

rotating back into the global co-ordinate frame the g-tensor is sublattice dependent

$$\begin{aligned} \mathbf{g}_0 &= \begin{pmatrix} g_1 & g_2 & g_2 \\ g_2 & g_1 & g_2 \\ g_2 & g_2 & g_1 \end{pmatrix} & \mathbf{g}_1 &= \begin{pmatrix} g_1 & -g_2 & -g_2 \\ -g_2 & g_1 & g_2 \\ -g_2 & g_2 & g_1 \end{pmatrix} \\ \mathbf{g}_2 &= \begin{pmatrix} g_1 & -g_2 & g_2 \\ -g_2 & g_1 & -g_2 \\ g_2 & -g_2 & g_1 \end{pmatrix} & \mathbf{g}_3 &= \begin{pmatrix} g_1 & g_2 & -g_2 \\ g_2 & g_1 & -g_2 \\ -g_2 & -g_2 & g_1 \end{pmatrix} \end{aligned} \quad (\text{K4})$$

where

$$g_1 = \frac{2}{3}g_{xy} + \frac{1}{3}g_z \quad g_2 = -\frac{1}{3}g_{xy} + \frac{1}{3}g_z. \quad (\text{K5})$$

The structure factor $S(\mathbf{q})$ can also be resolved into spin flip (SF) and non-spin flip (NSF) components, for comparison with experiments carried out using polarised neutrons. For neutrons with polarisation along $\hat{\mathbf{n}}$, these are given by

$$S^{\text{NSF}}(\mathbf{q}) = \sum_{\alpha,\beta=1}^3 \sum_{i,j=1}^4 \langle (\mathbf{m}^i(-\mathbf{q}) \cdot \hat{\mathbf{n}})(\mathbf{m}^j(\mathbf{q}) \cdot \hat{\mathbf{n}}) \rangle \quad (\text{K6})$$

$$\begin{aligned} S^{\text{SF}}(\mathbf{q}) &= \sum_{\alpha,\beta=1}^3 \sum_{i,j=1}^4 \frac{1}{q^2} \langle (\mathbf{m}^i(-\mathbf{q}) \cdot (\hat{\mathbf{n}} \times \mathbf{q})) \\ &\quad \times (\mathbf{m}^j(\mathbf{q}) \cdot (\hat{\mathbf{n}} \times \mathbf{q})) \rangle \end{aligned} \quad (\text{K7})$$

Where we quote results for SF and NSF components of $S(\mathbf{q})$ below, we consider $\hat{\mathbf{n}} = (1, -1, 0)/\sqrt{2}$.

The correlation function $\langle m_{\alpha}^i(-\mathbf{q})m_{\beta}^j(\mathbf{q}) \rangle$ needed to evaluate $S(\mathbf{q})$ [Eq. (K1)] can be calculated directly from correlations of the spins $S_{\beta}(\vec{R}_i)$ in a classical Monte Carlo simulation. For ordered phases, it can also be calculated analytically within either the classical (low-T) or semi-classical (LSW) spin-wave approximations. In the case of the low-T expansion, discussed below, this makes use of the fact that $\langle m_{\alpha}^i(-\mathbf{q})m_{\beta}^j(\mathbf{q}) \rangle$ can be expressed in terms of

$$\langle v_{i\mathbf{q}} \tilde{v}_{j-\mathbf{q}} \rangle = \delta_{ij} \frac{T}{\kappa_{i\mathbf{q}}} \quad (\text{K8})$$

(c.f. Eq. (F13)).

2. Details of simulations

In Fig. 4 of the main text we show classical Monte Carlo simulation results for the equal-time structure factor $S(\mathbf{q})$, for a range of parameters associated with the non-collinear ferromagnet. These simulations were carried out for a cluster of $N = 27648$ spins ($L = 12$), with $t_{max} = 10^5$ MCs, and averaged over 10 independent samples. The figure is composed of 9216 pixels, each corresponding to one of the allowed \mathbf{q} -vectors in the $[hhl]$ plane for a cluster of this size. $S(\mathbf{q})$ was calculated following the definition Eq. (K1), using the measured g-tensor for $\text{Yb}_2\text{Ti}_2\text{O}_7$ ^{26,47}, with $g_{xy} = 4.18$ and $g_z = 1.77$. Since simulations were performed in the paramagnetic phase, at relatively high temperatures, neither parallel tempering nor over-relaxation were needed to obtain well-equilibrated results.

In Fig. 5 of the main text we show classical Monte Carlo simulation results for the equal-time structure factor $S(\mathbf{q})$, for a range of parameters associated with the Ψ_2 phase. Details of these simulations were exactly as for Fig. 4, described above. However in this case, the structure factor was calculated using the measured g-tensor for $\text{Er}_2\text{Ti}_2\text{O}_7$ ²⁸, with $g_{xy} = 5.97$ and $g_z = 2.45$.

3. Comparison of Monte Carlo simulation and spin wave theory

Here, to demonstrate the quality of our simulation data, we compare the structure factors, as calculated from the classical spin wave theory $\mathcal{H}_{\text{ex}}^{\text{CSW}}$ [Eq. (F12)] and Monte Carlo simulation, for three different parameter sets: the parameters of $\text{Yb}_2\text{Ti}_2\text{O}_7$ as found in Ref.²⁶ where the classical ground state is ferromagnetic, the parameters of $\text{Er}_2\text{Ti}_2\text{O}_7$ as found in Ref.²⁸ where we expect the order by disorder mechanism to favour the Ψ_2 states and one set of parameters where the order by disorder mechanism favours the Ψ_3 states. We find excellent, quantitative agreement between the two methods.

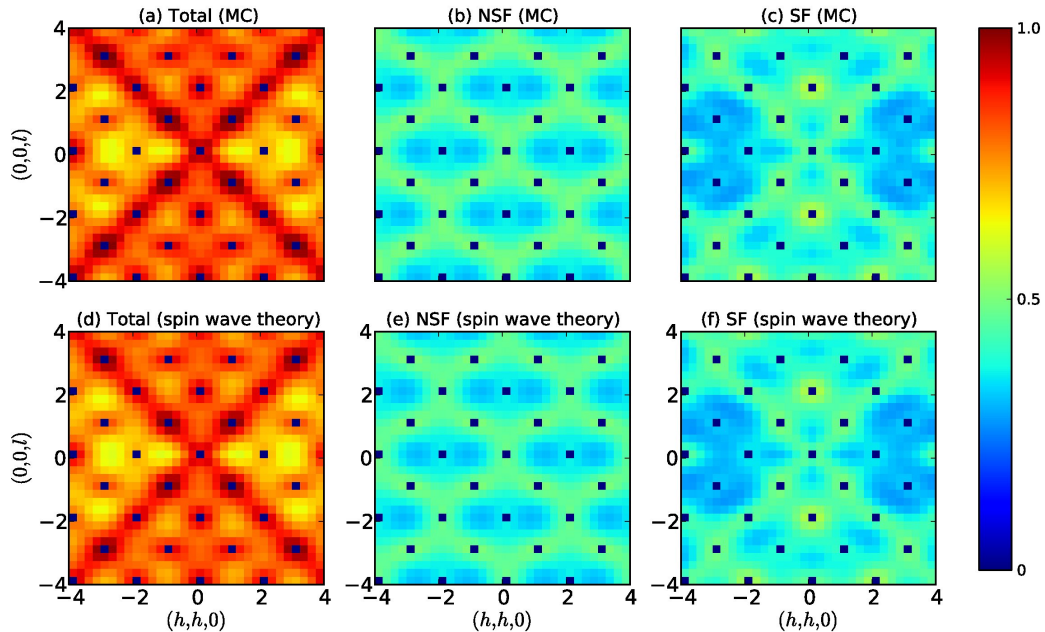


FIG. 22: Comparison between results for equal-time structure factor $S(\mathbf{q})$ obtained in classical Monte Carlo (MC) simulation and classical low-temperature expansion (spin wave theory) for parameters appropriate to $\text{Yb}_2\text{Ti}_2\text{O}_7$ ²⁶. a) Total scattering in the (h, h, l) plane within MC simulation. b) Associated scattering in the non spin-flip (NSF) channel. c) Associated scattering in the spin-flip (SF) channel. d) Total scattering in the (h, h, l) plane within a spin-wave expansion about the ferromagnetic ground state. e) Associated scattering in the NSF channel. f) Associated scattering in the SF channel. Rods of scattering in the (h, h, h) direction, associated with a low-energy spin-wave excitation, are visible in both SF and NSF channels. All results were obtained at $T = 0.05$ K, for exchange parameters $J_1 = -0.09\text{meV}$, $J_2 = -0.22\text{meV}$, $J_3 = -0.29\text{meV}$, setting $J_4 = 0$. SF and NSF channels are defined with respect to a neutron with polarisation in the $(1, -1, 0)$ direction, as in Ref. 61. $S(\mathbf{q})$ has been calculated using the experimentally measured g-tensor for $\text{Yb}_2\text{Ti}_2\text{O}_7$ ^{26,47}, with $g_z = 1.77$, $g_{xy} = 4.18$. In order to avoid saturating the colour scale, the spectral weight associated with Bragg peaks at reciprocal lattice vectors has been subtracted.

In Fig. 22 we show the structure factor $S(\mathbf{q})$ calculated both from classical spin wave theory and from Monte Carlo simulation at $T = 0.05\text{K}$, in the NSF, SF and total scattering channels (see Eqs. (K1), (K6) and (K7)). We have used the experimentally determined parameters for the g-tensor⁴⁷ $g_z = 1.77$, $g_{xy} = 4.18$ and exchange integrals²⁶ $J_1 = -0.09\text{meV}$, $J_2 = -0.22\text{meV}$ and $J_3 = -0.29\text{meV}$, setting $J_4 \equiv 0$. Rod-like features are clearly visible in the total scattering along $[111]$ directions. These are associated with a low-energy spin-wave mode which disperses very weakly in the $[111]$ direction [cf. Fig. 15]. The excellent, quantitative agreement between spin wave theory and simulation demonstrates the excellent equilibration of the simulations down to 0.05K for the parameters of $\text{Yb}_2\text{Ti}_2\text{O}_7$, and strongly supports our understanding of the origin of the rod-like features seen in neutron scattering [20,44–46,48].

$S(\mathbf{q})$ is also useful for studying the entropic ground state selection within the one-dimensional manifold of state with E symmetry. For a given set of parameters we may compare the diffuse scattering calculated in spin wave theory in expansions around the Ψ_3 and Ψ_2 phases

with the diffuse scattering calculated in simulations.

Such a comparison is shown in Fig. 23, for exchange parameters appropriate to $\text{Er}_2\text{Ti}_2\text{O}_7$ ($J_1 = 0.11$ meV, $J_2 = -0.06$ meV and $J_3 = -0.10$ meV, setting $J_4 \equiv 0$) and temperature $T = 0.36\text{K}$. From the entropy calculations shown in Fig. 16 we expect the Ψ_2 state to be preferred for these values of the exchange parameters. Comparison of the distribution of weight in the vicinity of the $(1, 1, 1)$, $(3, 3, 3)$ and $(1, 1, 3)$ reciprocal lattice vectors between the Monte Carlo data and the spin wave expansions around the Ψ_2 and Ψ_3 phases supports this conclusion.

Similarly, in Fig. 24 we show a comparison of the diffuse scattering between Monte Carlo simulations and spin wave expansions around the Ψ_2 and Ψ_3 phases for exchange parameters approaching the non-collinear ferromagnetic phase ($J_1 = 0$, $J_2 = -1.0$ meV and $J_3 = -0.1$ meV, $J_4 = 0$), at $T = 0.4\text{K}$. Calculations of the entropy within spin wave theory show that the Ψ_3 state should be preferred by fluctuations for these parameters, and this is confirmed by the comparison of the structure factors, in particular by the presence of bright

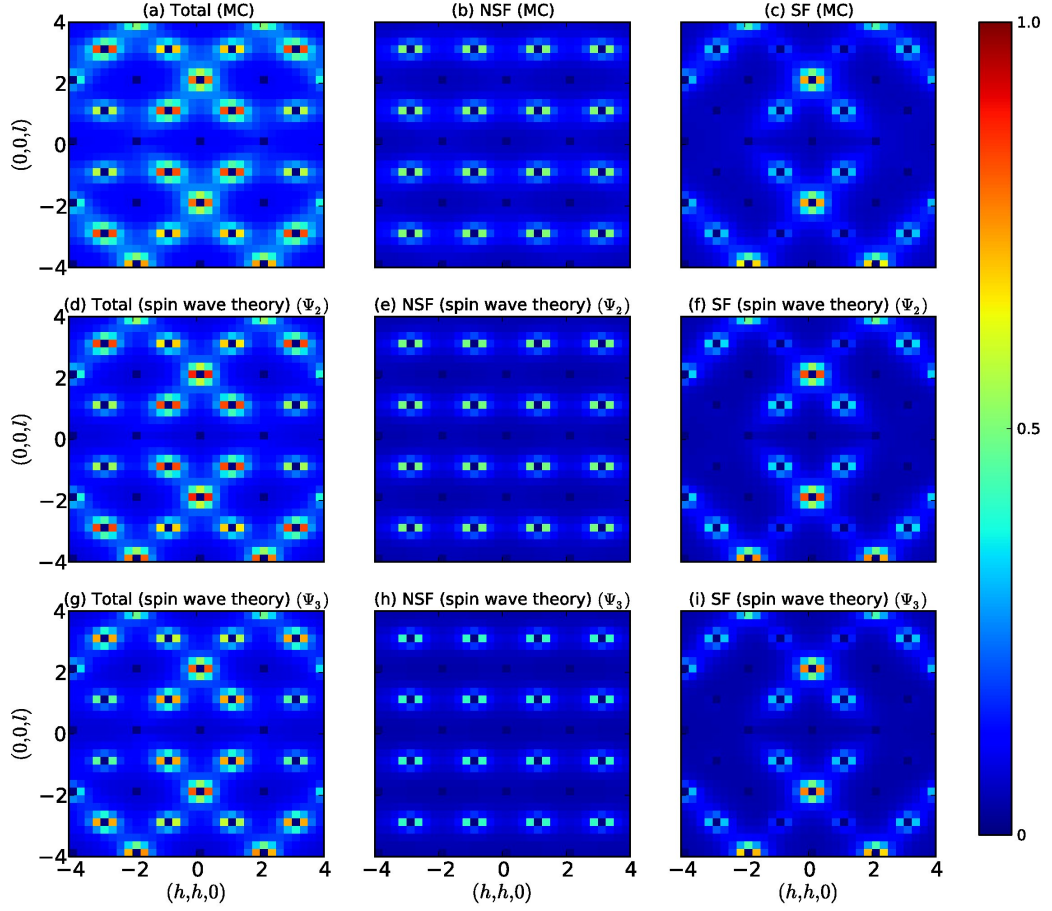


FIG. 23: Comparison between results for equal-time structure factor $S(\mathbf{q})$ obtained in classical Monte Carlo (MC) simulation and low-temperature expansion (classical spin wave theory) for parameters appropriate to $\text{Er}_2\text{Ti}_2\text{O}_7$. a) Total scattering in the (h, h, l) plane within MC simulation. b) Associated scattering in the non spin-flip (NSF) channel. c) Associated scattering in the spin-flip (SF) channel. d) Total scattering in the (h, h, l) plane within a spin-wave expansion about a Ψ_2 ground state. e) Associated scattering in the NSF channel. f) Associated scattering in the SF channel. g) Total scattering in the (h, h, l) plane within a spin-wave expansion about a Ψ_3 ground state. h) Associated scattering in the NSF channel. i) Associated scattering in the SF channel. Careful comparison of the distribution of scattering in the vicinity of the $(1, 1, 1)$, $(3, 3, 3)$ and $(1, 1, 3)$ reciprocal lattice vectors supports the conclusion that the Ψ_2 state is preferred for these exchange parameters, in agreement with experiment and the calculations described in the text. All results were obtained at $T = 0.36$ K, for exchange parameters $J_1 = 0.11$ meV, $J_2 = -0.06$ meV, $J_3 = -0.10$ meV, setting $J_4 \equiv 0$ [28]. For clarity, spectral weight associated with Bragg peaks at reciprocal lattice vectors has been subtracted.

rods in the $[111]$ direction.

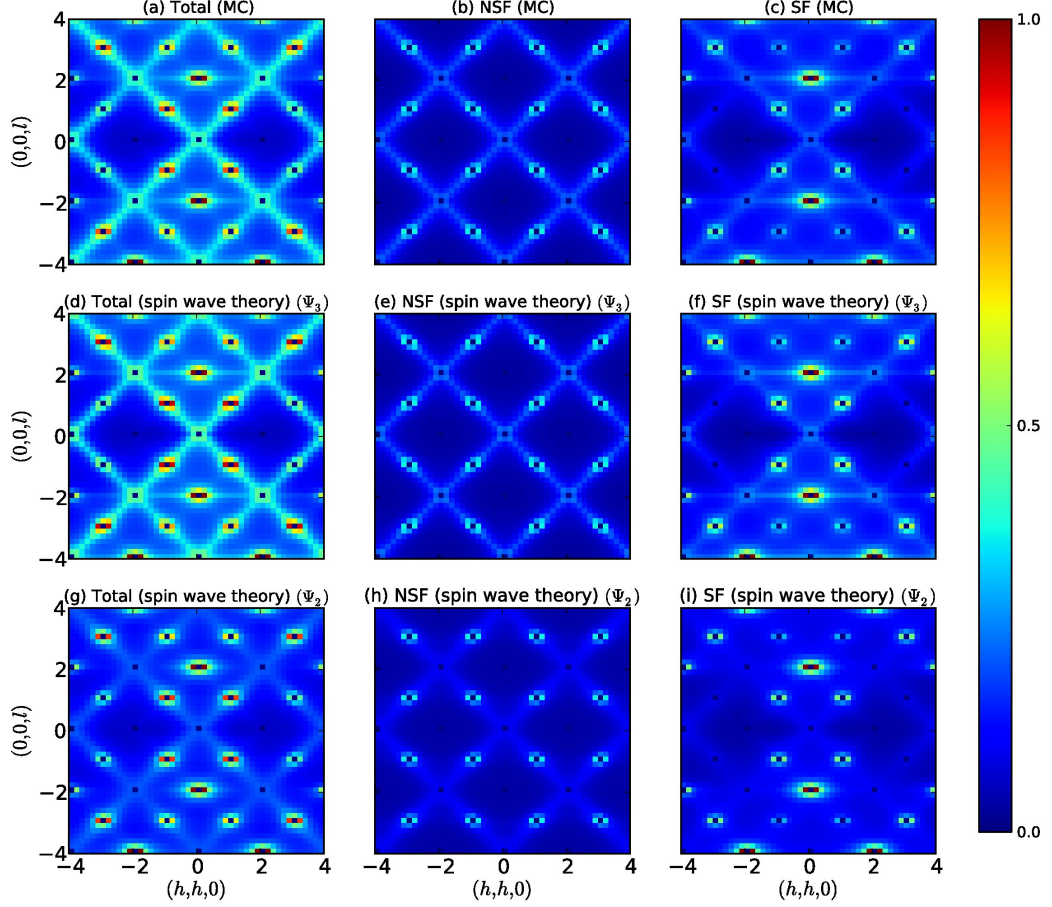


FIG. 24: Comparison between results for equal-time structure factor $S(\mathbf{q})$ obtained in classical Monte Carlo (MC) simulation and low-temperature expansion (classical spin wave theory) in the ordered phase for parameters $J_1 = 0$, $J_2 = -1.0$ meV, $J_3 = -0.10$ meV, $J_4 \equiv 0$, approaching the non-collinear ferromagnet from within the E-symmetry phase. a) Total scattering in the (h, h, l) plane within MC simulation showing strong rod-like features in $[111]$ directions. b) Associated scattering in the non spin-flip (NSF) channel. c) Associated scattering in the spin-flip (SF) channel. d) Total scattering in the (h, h, l) plane within a classical spin-wave expansion about a Ψ_3 ground state, showing strong rod-like features in $[111]$ directions. e) Associated scattering in the NSF channel. f) Associated scattering in the SF channel. g) Total scattering in the (h, h, l) plane within a classical spin-wave expansion about a Ψ_2 ground state. h) Associated scattering in the NSF channel. i) Associated scattering in the SF channel. Comparison of the scattering supports the conclusion that the Ψ_3 ground state is found in simulation, in agreement with the results of the low-T expansion [cf. Fig. 16]. An isotropic g-tensor $g_z = 1, g_{xy} = 1$ has been assumed. For clarity, spectral weight associated with Bragg peaks at reciprocal lattice vectors has been subtracted.

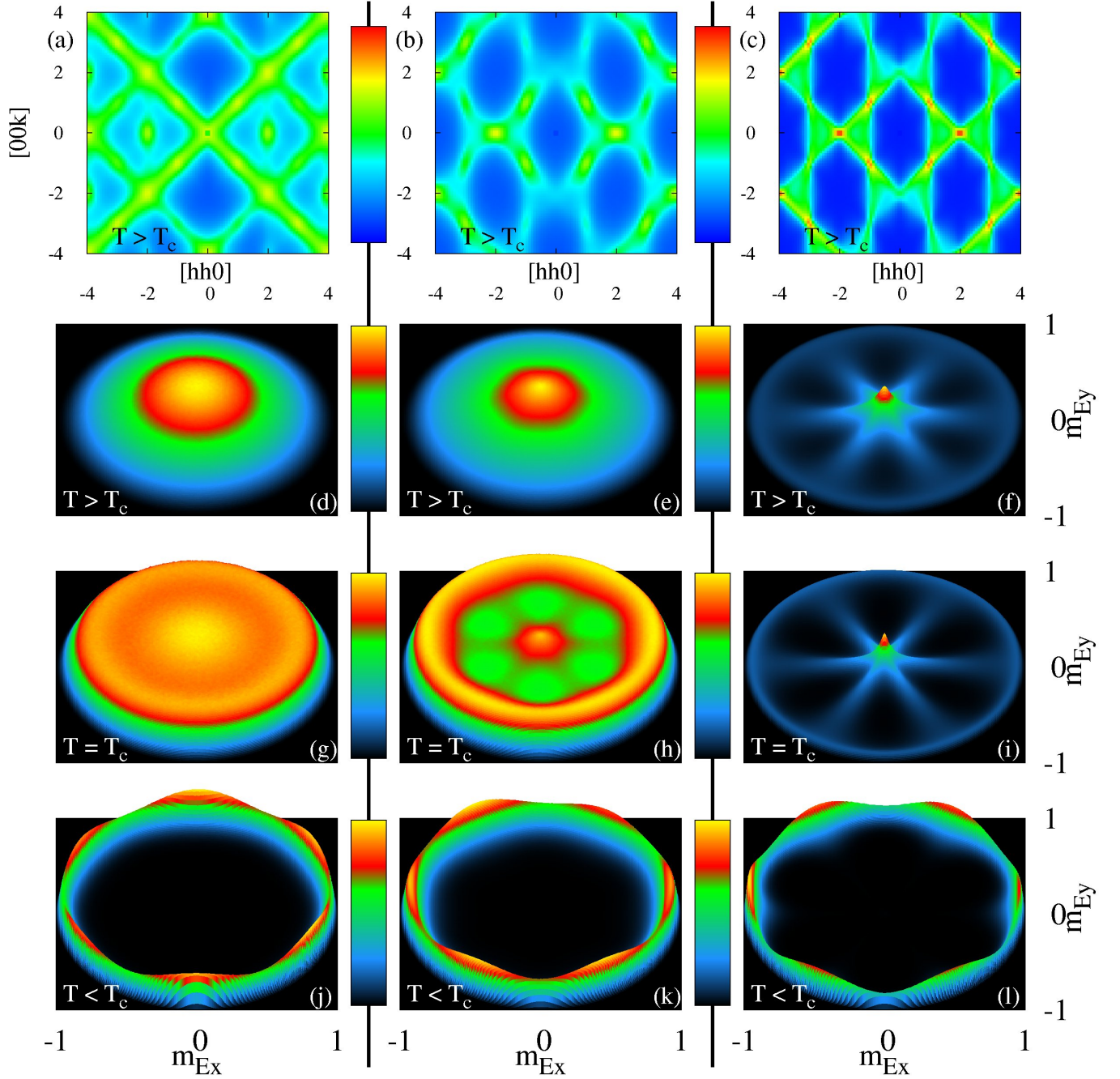


FIG. 25: Influence of ground-state degeneracy on finite-temperature phase transitions, as revealed by the probability distribution of the order parameter $\mathbf{m}_E = m_E (\cos \theta_E, \sin \theta_E)$ [Eq. (D8)]. Results are taken from simulation of \mathcal{H}_{ex} [Eq. (A2)], with parameters chosen correspond to (1) a Ψ_3 ground state, approaching the non-collinear FM (a, d, g, j) with $T_c = 0.39$ K; (2) a Ψ_2 ground state (b, e, h, k) with $T_c = 0.26$ K; (3) a Ψ_2 ground state, on the border of the Palmer-Chalker phase (c, f, i, l) with $T_c = 0.065$ K. (a)-(c) quasi-elastic scattering $S(\mathbf{q})$ in the paramagnetic phase $T > T_c$. (d)-(f) corresponding results for the probability density function, $P(\mathbf{m}_E)$. (g)-(i) $P(\mathbf{m}_E)$ at the transition temperature $T = T_c$. (j)-(l) $P(\mathbf{m}_E)$ in the ordered phase $T < T_c$. (1) For a finite-size system, the onset of Ψ_3 occurs progressively, through (g) the emergence of a one-dimensional manifold of states with finite $|\mathbf{m}_E|$, and then (j) the entropic selection of θ_E corresponding to one of six distinct Ψ_3 ground states. (a) The connection with the non-collinear FM is evident in $S(\mathbf{q})$, with rods of scattering strongly reminiscent of those seen in $\text{Yb}_2\text{Ti}_2\text{O}_7$. (2) The same process occurs, but in this case $P(\mathbf{m}_E)$ shows Ψ_2 ground states are favoured at low temperatures (k) and even at the transition (h). (3) On the boundary of the Palmer-Chalker phase, the ground state manifold includes additional manifolds of states which mix \mathbf{m}_E and \mathbf{m}_{T_2} . These are evident (i) in the “spoked wheel” seen in $P(\mathbf{m}_E)$ at $T = T_c$, and drive the entropic selection of the Ψ_2 ground state. (c) The high degeneracy at this phase boundary is also evident in the “bow-tie” structure in $S(\mathbf{q})$. Further details of simulations and parameters for (1), (2) and (3) are given in the text.

Appendix L: Living on the edge : the influence of ground state manifolds on finite-temperature phase transitions

The major assertion of this article is that many of the interesting properties of pyrochlore magnets — for example the rods of scattering observed in $\text{Yb}_2\text{Ti}_2\text{O}_7$, and the order-by-disorder selection of a Ψ_2 ground state in $\text{Er}_2\text{Ti}_2\text{O}_7$ — are the direct consequence of the high ground-state degeneracy where phases with different symmetry meet. While the arguments for enlarged ground state manifolds at $T = 0$ are easy to understand, it is far less obvious that this degeneracy should make itself felt at finite temperature, especially where it is not protected by symmetry.

We can test the internal consistency of these ideas by using the probability distribution of the order parameter

$$\mathbf{m}_E = m_E (\cos \theta_E, \sin \theta_E)$$

[cf. Eq. (D8)] to deconstruct the order-by-disorder selection of Ψ_2 and Ψ_3 ground states in finite-temperature simulations of \mathcal{H}_{ex} [Eq. (A2)]. The probability density function $P(\mathbf{m}_E)$ is sensitive both to the formation of a one-dimensional manifold of states with E symmetry — which manifests itself as a ring in $P(\mathbf{m}_E)$ — and to the selection of an ordered ground state within this manifold — which will appear as six degenerate maxima within the ring.

$P(\mathbf{m}_E)$ also enables us to study the evolution of the ground state manifolds at the boundaries between phases with competing symmetry — in this case \mathbf{m}_{Γ_2} and $\mathbf{m}_{\Gamma_{1A'}}$. At these phase boundaries, \mathbf{m}_E takes on a new, constrained set of values, characteristic of the way in which different manifolds connect. For example Eq. (E4–E6) predicts that, on the boundary with the Palmer-Chalker phase, the one-dimensional manifold of states with $|\mathbf{m}_E| = 1$ acquires “spokes” in the directions

$$\theta_E = \left\{ 0, \frac{\pi}{3}, \frac{2\pi}{3}, \pi, \frac{4\pi}{3}, \frac{5\pi}{3} \right\}$$

connecting $\mathbf{m}_E = 0$ with the six Ψ_2 ground states. Observation of such a “spinning wheel” pattern in $P(\mathbf{m}_E)$ at finite temperature would therefore confirm that the zero-temperature degeneracies were still operative.

In Fig. 25 we present results for $P(\mathbf{m}_E)$ and $S(\mathbf{q})$ taken from simulations of \mathcal{H}_{ex} [Eq. (A2)] for three sets of parameters

$$(1) \quad (J_1, J_2, J_3, J_4) = (0, -0.3, -0.1, 0) \quad \text{meV}$$

where we expect a Ψ_3 ground state, but are approaching the border with the non-collinear FM [Fig. 25 (a, d, g, j)];

$$(2) \quad (J_1, J_2, J_3, J_4) = (0.11, 0.06, -0.1, 0) \quad \text{meV}$$

where we expect a Ψ_2 ground state, but are approaching the border with the Palmer-Chalker phase [Fig. 25 (b, e, h, k)]; and

(3) $(J_1, J_2, J_3, J_4) = (0.11, 0.11, -0.1, 0)$ meV exactly on the $T = 0$ border of the Palmer-Chalker phase [Fig. 25 (c, f, i, l)].

The results for $S(\mathbf{q})$ shown in Fig. 25(a-c), demonstrate the diffuse structure expected in the paramagnet in each case : (1) Fig. 25(a) — rods of scattering, reminiscent of those observed in $\text{Yb}_2\text{Ti}_2\text{O}_7$ [20,44–46,48]; (2) Fig. 25(b) — a diffuse web of rings, reminiscent to that observed in experiments on $\text{Er}_2\text{Ti}_2\text{O}_7$ [42], also ordering in Ψ_2 ; (3) Fig. 25(c) — “bow-tie” patterns reminiscent of the pinch points observed in the Heisenberg antiferromagnet on a pyrochlore lattice [62,63],

The corresponding results for $P(\mathbf{m}_E)$ in the paramagnet show a broad distribution of \mathbf{m}_E , consistent with fluctuations in the absence of order, for both parameter sets (1) [Fig. 25(d)]. However on the border of the Palmer-Chalker phase (3) [Fig. 25(f)] $P(\mathbf{m}_E)$ shows a diffuse spoked wheel, confirming that the connection implied by the $T = 0$ ground state manifold survives at finite temperature. The \mathbb{Z}_6 symmetry actually also transpires at finite temperature for parameter sets (2) [Fig. 25(h)], indicating that the $T = 0$ ground state degeneracy on the boundaries can be felt even in the paramagnetic regime away from the boundaries. The reason why we see it at $T_c = 0.26$ K for parameter set (2) and not at $T_c = 0.39$ K for parameter set (1) is probably a consequence of the strong finite size dependence of the entropic selection between Ψ_2 and Ψ_3 .

¹ L. Balents Nature **464**, 199 (2010).

² C. Castelnovo, R. Moessner, and S. L. Sondhi, Annu. Rev. Cond. Mat. Phys. **3**, 35 (2012).

³ M. Hermele, M. P. A. Fisher, and L. Balents, Phys. Rev. B **69**, 064404 (2004).

⁴ A. Banerjee, S. V. Isakov, K. Damle, and Y.-B. Kim, Phys. Rev. Lett. **100**, 047208 (2008).

⁵ L. Savary and L. Balents, Phys. Rev. Lett. **108**, 037202 (2012).

⁶ N. Shannon, O. Sikora, F. Pollmann, K. Penc, and P.

Fulde, Phys. Rev. Lett. **108**, 067204 (2012)

⁷ O. Benton, O. Sikora, and N. Shannon, Phys. Rev. B **86**, 075154 (2012),

⁸ S.-B. Lee, S. Onoda and L. Balents, Phys. Rev. B **86**, 104412 (2012)

⁹ L. Savary and L. Balents, Phys. Rev. B **87**, 205130 (2013)

¹⁰ H. W. J. Blöte, R. F. Wierlinga and W. J. Huiskamp, Physica **43**, 549 (1969)

¹¹ J. S. Gardner, M. J. P. Gingras, and J. E. Greedan, Rev. Mod. Phys. **82**, 53 (2010).

- ¹² J. S. Gardner, S. R. Dunsiger, B. D. Gaulin, M. J. P. Gingras, J. E. Greedan, R. F. Kiefl, M. D. Lumsden, W. A. MacFarlane, N. P. Raju, J. E. Sonier, I. Swainson and Z. Tun, *Phys. Rev. Lett* **92**, 1012-1015 (1999)
- ¹³ I. Mirebeau, I. N. Goncharenko, P. Cadavez-Pares, S. T. Bramwell, M. J. P. Gingras, and J. S. Gardner, *Nature* **420**, 54 (2002).
- ¹⁴ K. Matsuhira, Y. Hinatsu, K. Tenya, H. Amitsuka and T. Sakakibara, *J. Phys. Soc. Jpn.* **71**, 1576, (2002).
- ¹⁵ J. Lago, T. Lancaster, S. J. Blundell, S. T. Bramwell, F. L. Pratt, M. Shirai and C. Baines, *J. Phys.: Condens. Matter* **17**, 979, (2005).
- ¹⁶ Masae Shirai, *Experimental Investigations of Frustrated Magnets*, Thesis(PhD)–University of London, 2007.
- ¹⁷ P. M. Sarte, H. J. Silverstein, B. T. K. van Wyk, J. S. Gardner, Y. Qiu, H. D. Zhou and C. R. Wiebe, *J. Phys.: Condens. Matter* **23**, 382201, (2011).
- ¹⁸ S. Guitteny, S. Petit, E. Lhotel, J. Robert, P. Bonville, A. Forget and I. Mirebeau, *Phys. Rev. B* **88**, 134408, (2013).
- ¹⁹ J. D. M. Champion, M. J. Harris, P. C. W. Holdsworth, A. S. Wills, G. Balakrishnan, S. T. Bramwell, E. Cizmar, T. Fennell, J. S. Gardner, J. Lago, D. F. McMorro, M. Orendac, A. Orendacova, D. McK. Paul, R. I. Smith, M. T. F. Telling, and A. Wildes *Phys. Rev. B* **68**, 020401(R), (2003)
- ²⁰ K. A. Ross, J. P. C. Ruff, C. P. Adams, J. S. Gardner, H. A. Dabkowska, Y. Qiu, J. R. D. Copley, and B. D. Gaulin, *Phys. Rev. Lett.* **103**, 227202 (2009).
- ²¹ R. Siddharthan, B. S. Shastry, A. P. Ramirez, A. Hayashi, R. J. Cava, and S. Rosenkranz, *Phys. Rev. Lett.* **83**, 1854 (1999).
- ²² B. C. den Hertog and M. J. P. Gingras, *Phys. Rev. Lett.* **84**, 3430 (2000).
- ²³ H. B. Cao, A. Gukasov, I. Mirebeau, and P. Bonville, *J. Phys.: Condens. Matter* **21**, 492202 (2009).
- ²⁴ S. H. Curnoe, *Phys. Rev. B* **75**, 212404 (2007); *ibid.* **76**, 139903(E) (2007);
- ²⁵ P. A. McClarty, S. H. Curnoe and M. J. P. Gingras, *J. Phys.: Conf. Series* **145**, 012032 (2009);
- ²⁶ K. A. Ross, L. Savary, B. D. Gaulin, and L. Balents, *Phys. Rev. X* **1**, 021002 (2011).
- ²⁷ R. Applegate, N. R. Hayre, R. R. P. Singh, T. Lin, A. G. R. Day and M. J. P. Gingras *Phys. Rev. Lett.* **109**, 097205 (2012)
- ²⁸ L. Savary, K. A. Ross, B. D. Gaulin, J. P. C. Ruff, and L. Balents, *Phys. Rev. Lett.* **109**, 167201 (2012)
- ²⁹ M. E. Zhitomirsky, M. V. Gvozdkova, P. C. W. Holdsworth, and R. Moessner, *Phys. Rev. Lett.* **109**, 077204 (2012).
- ³⁰ J. Oitmaa, R. R. P. Singh, A. G. R. Day, B. V. Bagheri and M. J. P. Gingras, arXiv:1305.2935v1
- ³¹ M. J. Harris, S. T. Bramwell, D. F. McMorro, T. Zeiske, and K. W. Godfrey, *Phys. Rev. Lett.* **79**, 2554 (1997).
- ³² A. P. Ramirez, A. Hayashi, R. J. Cava, R. Siddharthan and B. S. Shastry, *Nature* **399**, 3335 (1999).
- ³³ D. Pomaranski, L. R. Yaraskavitch, S. Meng, K. A. Ross, H. M. L. Noad, H. A. Dabkowska, B. D. Gaulin and J. B. Kycia, *Nature Phys.* **9**, 353 (2013).
- ³⁴ B. Canals and C. Lacroix, *Phys. Rev. Lett.* **80**, 2933 (1998)
- ³⁵ P. H. Conlon and J. T. Chalker, *Phys. Rev. Lett* **102**, 237206 (2009).
- ³⁶ A. Poole, A. S. Wills and E. Lelièvre-Berna, *J. Phys.: Condens. Matter* **19**, 452201 (2007).
- ³⁷ O.V. Kovalev, *Representations of the Crystallographic Space Groups*, ed. 2, Gordon and Breach Science Publishers, Switzerland, 1993.
- ³⁸ S. E. Palmer and J. T. Chalker, *Phys. Rev. B* **62**, 488 (2000).
- ³⁹ A. Yaouanc, P. Dalmas de Réotier, P. Bonville, J. A. Hodges, V. Glazkov, L. Keller, V. Sikolenko, M. Bartkowiak, A. Amato, C. Baines, P. J. C. King, P. C. M. Gubbens and A. Forget *Phys. Rev. Lett.* **110**, 127207 (2013).
- ⁴⁰ S. T. Bramwell, M. J. P. Gingras, and J. N. Reimers, *J. Appl. Phys.* **75**, 5523 (1994).
- ⁴¹ J. D. M. Champion and P. C. W. Holdsworth, *J. Phys.: Condens. Matter* **16**, S665 (2004).
- ⁴² P. Dalmas de Réotier, A. Yaouanc, Y. Chapuis, S. H. Curnoe, B. Grenier, E. Ressouche, C. Marin, J. Lago, C. Baines and S. R. Giblin, *Phys. Rev. B* **86**, 104424 (2012).
- ⁴³ A. W. C. Wong, Z. Hao and M. J. P. Gingras, *Phys. Rev. B* **88**, 144402 (2013),
- ⁴⁴ K. A. Ross, L. R. Yaraskavitch, M. Laver, J. S. Gardner, J. A. Quilliam, S. Meng, J. B. Kycia, D. K. Singh, T. Proffen, H. A. Dabkowska, and B. D. Gaulin, *Phys. Rev. B* **84**, 174442 (2011).
- ⁴⁵ P. Bonville, J. A. Hodges, E. Bertin, J.-P. Bouchaud, P. Dalmas de Reotier, L.-P. Regnault, H. M. Ronnow, J.-P. Sanchez, S. Sosin, and A. Yaouanc, *Hyperfine Interact.* **156/157**, 103 (2004).
- ⁴⁶ J. D. Thompson, P. A. McClarty, H. M. Ronnow, L. P. Regnault, A. Sorge, and M. J. P. Gingras, *Phys. Rev. Lett.* **106**, 187202 (2011).
- ⁴⁷ J. A. Hodges, P. Bonville, A. Forget, M. Rams, K. Krolas and G. Dhalenne, *J. Phys.: Condens. Matter* **13**, 9301-9310 (2001).
- ⁴⁸ L.-J. Chang, S. Onoda, Y. Su, Y.-J. Kao, K.-D. Tsuei, Y. Yasui, K. Kakurai, and M. R. Lees, *Nat. Commun.* **3**, 992 (2012).
- ⁴⁹ R. M. D’Ortenzio, H. A. Dabkowska, S. R. Dunsiger, B. D. Gaulin, M. J. P. Gingras, T. Goko, J. B. Kycia, L. Liu, T. Medina, T. J. Munsie, D. Pomaranski, K. A. Ross, Y. J. Uemura, T. J. Williams and G. M. Luke, arXiv:1303.3850v1
- ⁵⁰ K. A. Ross, T. Proffen, H. A. Dabkowska, J. A. Quilliam, L. R. Yaraskavitch, J. B. Kycia and B. D. Gaulin, *Phys. Rev. B* **86**, 174424 (2012).
- ⁵¹ A. Poole, A. S. Wills and E. Lelièvre-Berna, *J. Phys.-Condens. Mat.* **19**, 452201 (2007), URL <http://stacks.iop.org/0953-8984/19/i=45/a=452201>.
- ⁵² B. Canals, M. Elhajal and C. Lacroix, *Phys. Rev. B* **78**, 214431 (2008).
- ⁵³ G. Chern, arXiv:1008.3038 (2010).
- ⁵⁴ N. Shannon, K. Penc and Y. Motome, *Phys. Rev. B* **81**, 184409 (2010).
- ⁵⁵ M. Roger, J. H. Hetherington and J. M. Delrieu, *Rev. Mod. Phys.* **55**, 1, (1983).
- ⁵⁶ R. H. Swendsen and J.-S. Wang, *Phys. Rev. Lett.* **57**, 2607 (1986), URL <http://link.aps.org/doi/10.1103/PhysRevLett.57.2607>.
- ⁵⁷ C. J. Geyer, *Computing Science and Statistics: Proceedings of the 23rd Symposium on the Interface* p. 156 (1991).
- ⁵⁸ M. Creutz, *Phys. Rev. D* **36**, 515 (1987), URL <http://link.aps.org/doi/10.1103/PhysRevD.36.515>.
- ⁵⁹ G. Marsaglia, *Ann. Math. Stat.* **43**, 645 (1972).
- ⁶⁰ K. Kanki, D. Loison and K. Schotte, *Eur. Phys. J. B* **44**, 309 (2005).
- ⁶¹ T. Fennell, P. P. Deen, A. R. Wildes, K. Schmalzl, D. Prab-

hakaran, A. T. Boothroyd, R. J. Aldus, D. F. McMorrow and S. T. Bramwell, *Science* **326**, 411 (2009).

⁶² R. Moessner and J. T. Chalker, *Phys. Rev. B* **58**, 12049 (1998)

⁶³ P. H. Conlon and J. Chalker, *Phys. Rev. B* **81**, 224413 (2010)